University of California, Santa Barbara

Bachelor's Honors Thesis

Development of Hardware for Scaling Up Superconducting Qubits and Simulation of Quantum Chaos

Author:
Michael Fang

Supervisor:
Dr. John Martinis

A thesis submitted in fulfilment of the requirements
for the degree of Bachelor of Science

in the

Martinis Group
Department of Physics

June 12, 2015

The dissertation of Michael Fang is approved:

John M. Martinis

June 2015

Contents

Chapter 1

Introduction and Motivation

In recent years, analog and digital quantum simulation using superconducting qubits has become a reality [1][2][3]. The field of experimental quantum computing is making steady progress towards the realization of a machine that can solve a certain class of problems exponentially faster than classical computers. However, quantum computation relies on the manipulation of fragile quantum states which are sensitive to unwanted excitations from the noisy environment. Isolating qubits from the surrounding environment will preserve the fidelity of quantum states.

In an experimental setting, qubits are not perfect or well isolated and the fidelity of quantum states degrades over time. Noise from the environment is leaked into a system of qubits through unwanted coupling between electrons and parasitic phonon or photons.

Parasitic phonons will couple with electrons above 20 mK and deflect the electron's free path in the superconducting layer. These deflections lead to dissipative loss found in normal conductors. Qubit experiments must remain below 20mK with isolation from vibrational sources, e.g. phonons generated by a pulse tube cryostat in a cryogen-free dilution refrigerator (DR). With tens of qubits, a thermal anchoring system must effectively transfer unwanted heat from hundreds of coaxial cables. Vacuum grease will be placed between the thermal anchor and cable to serve as a phononic bath for hot electrons. The rate of hot electrons thermalizing to the phononic bath should be much greater than the rate of hot electrons that remain thermalized to the cable.

Parasitic photons can leak into a DR and cause unwanted excitations in our system. From a photon's point of view, a DR has many available openings such as vacuum pump out ports, cryogenic cables, or telemetry wiring. Unlike phonons, photons will couple with electrons regardless of temperature. Stray light is controlled in three ways in a DR: black absorptive coating, microwave filters, and "light-tight" staging inside the DR. Impedance matched microwave filters preserve signal integrity and attenuate stray infrared photons. Filters based off of a epoxy mixture of bronze or copper powders are bulky, difficult to make, and have to be mounted such that valuable experimental space is taken up. Such filters limit the number of control lines we can use in our experiments and restricts the number of controllable qubits. As more qubits are added to our experiment, the need for a larger number of control lines in a compact form factor bsecomes paramount. Efficient and high performing microwave filters need to be developed to prevent a bottleneck in scaling up to a realizable quantum computer.

Although fault tolerant gate based quantum computation relies on millions of qubits, analog simulations of quantum systems are possible with a compatible architecture or Hamiltonian. With just three qubits, a spin 3/2 particle subjected to a non-linear periodic Hamiltonian can be realized with three transmons fully coupled via tunable couplers. The classical analog of this system exhibits chaotic motion whereas the time evolution of the quantum mechanical state is deterministic. Thus, it is surprising that measures of disorder for classical and quantum trajectories exhibit similar features in phase space.

This thesis will focus on isolating quantum systems from phononic and photonic noise, with a study on spin 3/2 quantum systems subjected to non-linear dynamics. The content of this thesis will assume basic knowledge of the experimental aspects of quantum computation using superconducting qubits.

Chapter 2

Development: Thermal Heat Sinking of Cryogenic Cables

Heat sinking coaxial cables at each stage of a dilution fridge is a critical task for maintaining the coherence of a qubit's quantum state. Any remaining heat in our system will allow thermal fluctuations to cause unwanted transitions in qubits. Transitions out of a qubit's original state mean lower coherence times, which prevent qubits from performing meaningful computations. A reliable and efficient heat sinking mount is needed. An implementation of such a heat sick is a cable clamp. A thin layer of vacuum grease lies between the cable and the clamp and relies on phonons to transfer thermal energy. A calculation for heat flow is carried out to assess the effectiveness of such a clamp, shown in Figure 2.2.

2.1 Thermal Physics

Fourier's Law gives the rate of heat transfer in watts. The rate of heat transfer is

$$P = -\kappa \oint_S \overrightarrow{\bigtriangledown} T \cdot d\overrightarrow{A}$$

where κ is the thermal conductivity and S is the surface of integration for heat flow. We can approximate a homogeneous material with radial symmetry as

$$P = -\kappa \frac{A}{\Delta x} \Delta T$$

with A the surface area enclosing the flux of heat flow and Δx the thickness of the temperature gradient across T_1 and T_2.

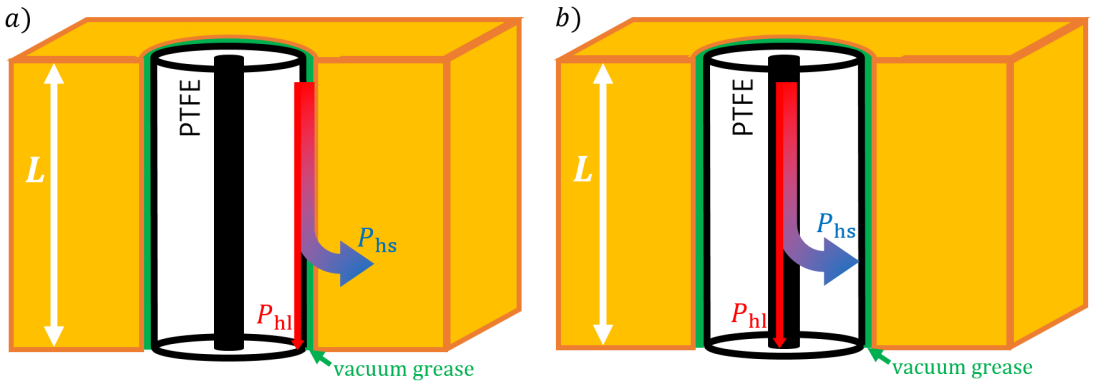

FIGURE 2.1: Diagram of a coaxial cable thermally anchored to a heat sink of length L. The heat sink power flow, P_{hs} is phononicly transfered out of the cable. The heat load power flow P_{hl} is electrically transfered down the cable.

2.2 External Conduction

First consider the interface between the outer conductor of the cable and the thermal anchor. There are two mechanisms (phononic and electronic) for heat conduction as shown in Fig. 2.1a). Phononic conduction serves as the heat sink and electronic conduction serves as the heat load. For an outer radius of the cable R_{outer}, thermal anchor length L, outer conductor thickness t_{cable}, and vacuum grease thickness t_{grease}, the power transfered for heat sinking and heat loading are:

$$P_{\text{hs}} = -\kappa_{\text{grease}} \frac{2\pi R_{\text{outer}} L}{t_{\text{grease}}} \Delta T$$

$$P_{\text{hl}} = -\kappa_{\text{cable}} \frac{2\pi R_{\text{outer}} t_{\text{cable}}}{L} \Delta T$$

The power ratio between the two mechanisms is

$$\frac{P_{\text{hs}}}{P_{\text{hl}}} = \frac{\kappa_{\text{grease}}}{\kappa_{\text{cable}}} \frac{L^2}{t_{\text{cable}} t_{\text{grease}}} \tag{2.1}$$

and approximates the device's efficiency. By referring to Fig. A.1 we can extrapolate conductivities for sub-Kelvin temperatures. For a cupronickel cable, $\kappa \approx 10^{-2}$ W/(m K). We use Apiezon N, which by Fig. A.1 has $\kappa \approx 10^{-5}$ W/(m K). For a 2.19 mm diameter cupronickel cable[1], vacuum grease thickness of 0.05 mm, and anchor clamping length of 10 mm, we find that $\frac{P_{\text{hs}}}{P_{\text{hl}}} \approx 7.5$.

2.3 Internal Conduction

If we were to now consider the interface between the center conductor to the outer conductor, we would have

$$\begin{aligned} P_{\text{hs}} &= -\kappa_{\text{teflon}} \frac{2\pi R_{\text{inner}} L}{t_{\text{teflon}}} \Delta T \\ P_{\text{hl}} &= -\kappa_{\text{cable}} \frac{\pi R_{\text{inner}}^2}{L} \Delta T \\ \frac{P_{\text{hs}}}{P_{\text{hl}}} &= \frac{\kappa_{\text{teflon}}}{\kappa_{\text{cable}}} \frac{2L^2}{R_{\text{inner}} t_{\text{teflon}}} \end{aligned} \tag{2.2}$$

For PTFE, we use $\kappa \approx 10^{-5}$. For a 2.19 mm diameter cupronickel cable, we find that $\frac{P_{\text{hs}}}{P_{\text{hl}}} \approx 1.5$ is much less effective than external conduction where $\frac{P_{\text{hs}}}{P_{\text{hl}}} \approx 7.5$. Thus, the overall process of transferring heat from the inner conductor to the thermal anchor is limited by the heat transfer from the inner conductor to the outer conductor. A more effective way to thermalize cables must be found to eliminate this bottleneck.

[1]The geometric properties of a 2.19 mm diameter cable from CoaxCo are found here: http://www.coax.co.jp/english/semi/219.html

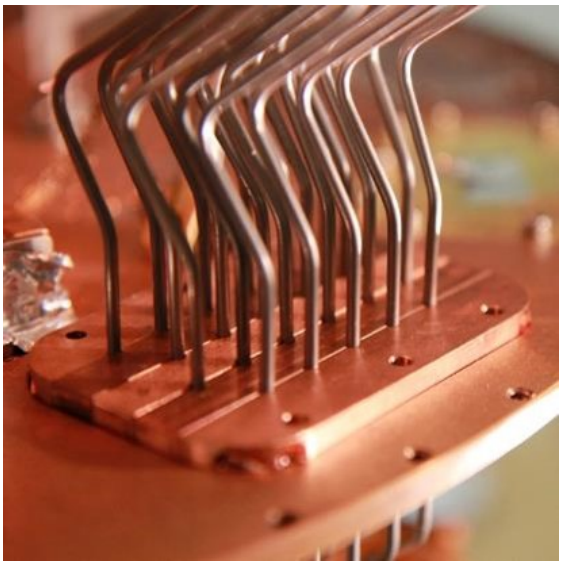

FIGURE 2.2

2.4 Improving Heat Sinking Efficiency

We explore other cable diameters and materials to improve the efficiency of thermal anchoring. The power ratio $\frac{P_{\text{hs}}}{P_{\text{hl}}}$ has two contributions. The first fraction in Eq. 2.1 and Eq. 2.2 governs the material properties of the cable for thermal conduction and is shown in Table 2.1 for various cable materials. The second fraction in Eq. 2.1 and Eq. 2.2 governs the geometric effects of thermal interfaces and is shown in Table 2.2 for various cable diameters.

TABLE 2.1: Material factors for various metals at 0.1 Kelvin. All thermal conductivities except NbTi approximated from Figure A.1. The value for NbTi is derived from CoaxCo's measurement [4].

Thermal Conductivities [W/(m K)] at 0.1 Kelvin				
PTFE	Apiezon N	Niobium	Cupronickel	Niobium Titanium
10^{-5}	10^{-5}	5×10^{-3}	10^{-2}	2×10^{-3}
Material Factor $\left(\frac{\kappa_{\text{grease}}}{\kappa_{\text{cable}}} = \frac{\kappa_{\text{teflon}}}{\kappa_{\text{cable}}}\right) \times 10^3$ **at 0.1 Kelvin**				
Niobium		Cupronickel		Niobium Titanium
2		1		5

TABLE 2.2: Geometric factors for various cable diameters and thermal transport mechanisms.

Cable Diameter	Inner Radius (R_{inner})	Teflon Thickness (t_{teflon})	Conductor Thickness (t_{cable})
0.860 mm	0.100 mm	0.230 mm	0.100 mm
1.600 mm	0.160 mm	0.365 mm	0.275 mm
2.190 mm	0.255 mm	0.580 mm	0.260 mm

	Geometric Factor $\times 10^{-3}$	
Cable Diameter	Internal Conduction $\left(\frac{L^2}{t_{\text{cable}} t_{\text{grease}}}\right)$	External Conduction $\left(\frac{2L^2}{R_{\text{inner}} t_{\text{teflon}}}\right)$
0.860 mm	20	8.7
1.600 mm	7.3	3.4
2.190 mm	7.7	1.4

Moving towards thinner cables will greatly increase the efficiency of heat sinking. The current cables in use (CuNi at 2.19 mm) can be improved by a factor of 13 and 31 for external and internal mechanisms respectively. These improvements are made with NbTi 0.86 mm cables and will give respective power ratios of 100 and 45 for external and internal conduction.

Chapter 3

Development: Infrared Filtering

Adding more qubits to our experiment increases the need for a larger number of control lines in a compact form factor. "Light tight" infrared filters on these control lines serve to block out infrared light which generate quasiparticles on our superconducting samples[5]. These quasiparticles act like dissipative metal conductors which negatively affect coherence times. New infrared filters were made to be compact while outperforming the previous generation of infrared filters.

The use of ECCOSORB load absorbers in infrared filters was influenced by filters made in Michel Devoret's Lab at Yale[6]. The product line of ECCOSORB absorbers are able to attenuate across a large frequency range (100 MHz - 100 GHz) depending on the application. For qubit control and measurement, filters with a low cutoff frequency are needed for Z control while filters with a high cutoff frequency are needed for XY control and readout.

High frequency filters should have little attenuation and low reflection at our operating point of 4 - 8 GHz. A length for attenuation of 1 cm is chosen so that attenuation is small at these frequencies. ECCOSORB CR-110, the least absorptive epoxy based product, will be used for these filters.

Low frequency filters are used on DC lines and attenuate strongly in the microwave

range. The attxenuation length is longer to achieve the same attenuation strength as the last generation of low frequency filters. ECCOSORB CR-124, the strongest epoxy based product, will be used for these filters. A low frequency filter can also be incorporated into the port of the mix plates, saving a considerable amount of space for more qubit experiments per dilution fridge.

3.1 Designing for Low Reflection

We can design a low reflection filter using the dielectric data provided on ECCOSORB's website[7]. For a coaxial cable of inner radius a and outer radius b with dielectric in between which has $\epsilon = \epsilon_0\epsilon_r$ and $\mu = \mu_0\mu_r$ [8]

$$L = \frac{\mu}{2\pi}\ln\left(\frac{b}{a}\right); \quad C = \frac{2\pi\epsilon}{\ln\left(\frac{b}{a}\right)}; \quad Z = \sqrt{\frac{L}{C}} \Rightarrow Z = \frac{376.7\Omega}{2\pi}\sqrt{\frac{\mu_r}{\epsilon_r}}\ln\left(\frac{b}{a}\right) \tag{3.1}$$

(Note: $\sqrt{\mu_0/\epsilon_0} = 376.7\Omega$)

As an example for MF-110 at 3 GHz[1], we have $\epsilon_r = 3.2$ and $\mu_r = 1.1$. Assuming $a = 30$ mil for 50Ω gives us $b = 124.4$ mil. The effects of dielectric loss become apparent at higher frequencies. Given loss tangents $\tan\delta_\epsilon$ and $\tan\delta_\mu$ or imaginary components μ_{im} and ϵ_{im} we have

$$Z = \frac{376.7\Omega}{2\pi}\sqrt{\frac{\mu_r\left(1 - i\tan\delta_\mu\right)}{\epsilon_r\left(1 - i\tan\delta_\epsilon\right)}}\ln\left(\frac{b}{a}\right) \quad \text{or} \quad Z = \frac{376.7\Omega}{2\pi}\sqrt{\frac{\mu_r - i\mu_{im}}{\epsilon_r - i\epsilon_{im}}}\ln\left(\frac{b}{a}\right) \tag{3.2}$$

[1]Note that ECCOSORB's CR line has the same dielectric properties as MF

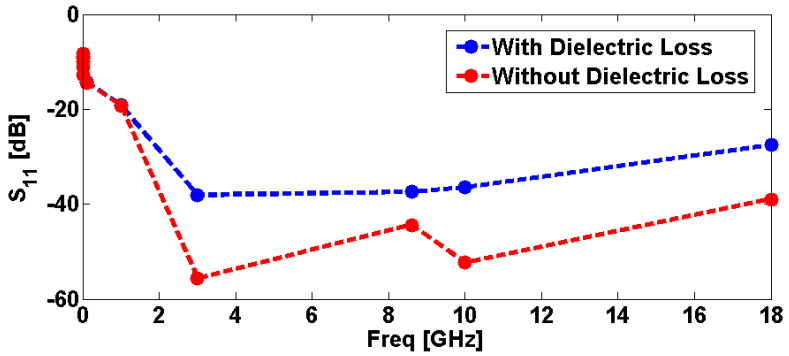

FIGURE 3.1: Reflection from a coaxial line with ECCOSORB CR-110, a = 30 mils, b = 125 mils. Two curves are shown: Considering dielectric loss in blue (Eq. 3.2) and not considering dielectric loss in red (Eq. 3.1). The dielectric data can be found at: [7]

The difference between considering and not considering dielectric loss for the ECCOSORB material is plotted in Figure 3.1, verifying that dielectric loss is an important parameter at high frequencies with reflection

$$|S11| = \left| \frac{Z - 50}{Z + 50} \right|. \tag{3.3}$$

Thus, we can minimize reflection (Eq. 3.3) up to high frequencies using this straightforward model as shown Figure 3.2, where we find islands of least reflection.

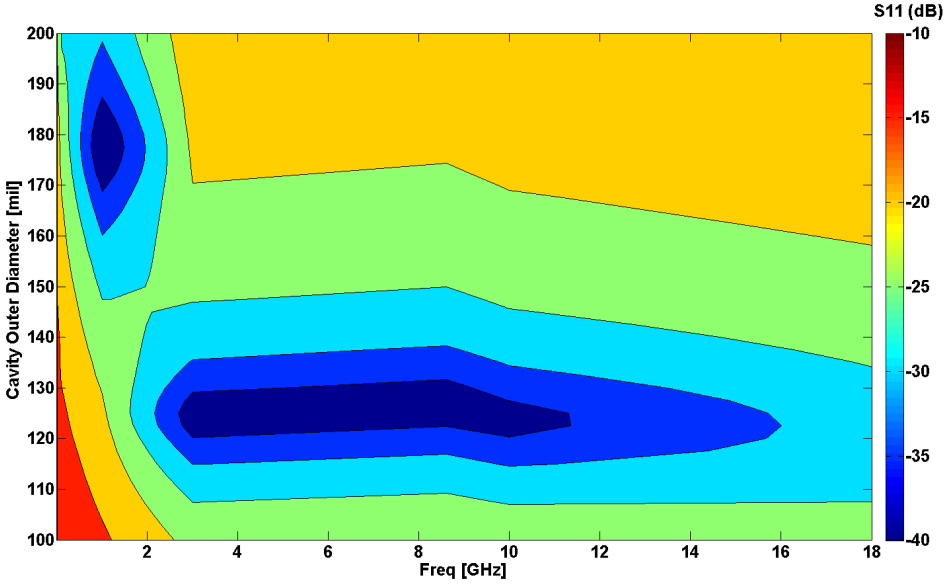

FIGURE 3.2: Simulated reflection with ECCOSORB CR-110 using an inner diameter a of 30 mils plotted over the outer diameter b and frequency. This contour plot was used to design the high frequency filter for low reflection. The best choice of b for the lowest reflection over a broad frequency is about 125 mils.

3.2 Parts List

The parts needed to make ECCOSORB filters are shown in Figure 3.3 and in addition the following equipment is needed: scale, clamp, hot plate, soldering iron, caliper, multimeter, and vacuum chamber for out-gassing.

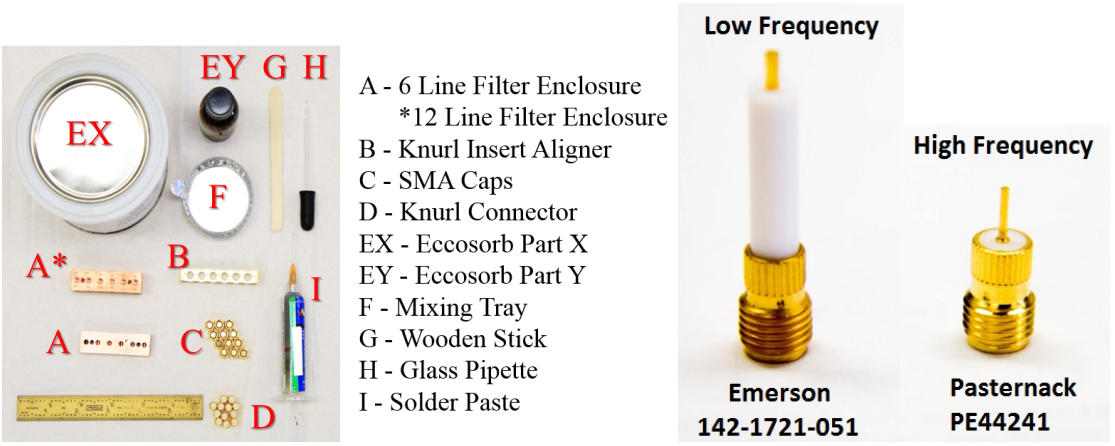

FIGURE 3.3: The SMA Cap (C) is Amphenol Connex 202112. If making high frequency filters, the SMA connector (D) is: Pasternack PE44241 (30 mil center pin). If making low frequency filters, the SMA connector (D) is: Emerson Network Power Connectivity Johnson 142-1721-051 (50 mil center pin). Make sure to strip off the extended Teflon dielectric from the low frequency connector.

The different variations of enclosures for high and low frequency filters are shown in Figure 3.4. It is **strongly recommended** to letter punch labels (before soldering) as shown on the cover page to distinguish between lines and filters.

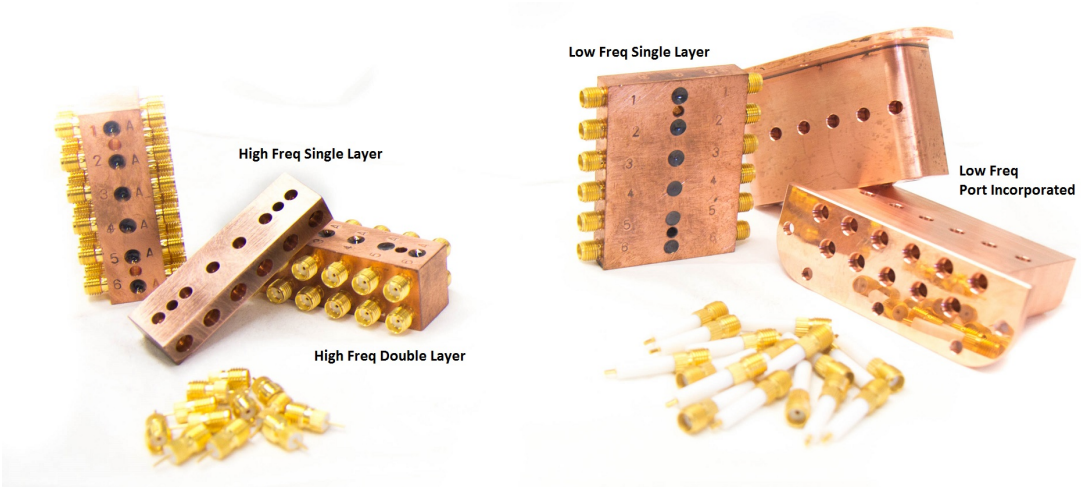

FIGURE 3.4: Left: High frequency filter enclosures including the single layer and double layer enclosures. Right: Low frequency filter enclosures including the single layer and two piece port incorporated enclosure

3.3 Assembly

There are three main steps of the assembly: 1. Inserting the knurl connectors into the enclosure and soldering two pins together and 2. Preparing the ECCOSORB absorber and 3. Injecting into the enclosure and curing. These filters can be assembled most efficiently with two people (one person each for step 1 and 2, together for 3). Note that step 1 may take shorter or longer than step 2 depending on how many connectors there are in the filter.

3.3.1 Step 1: Press Fit and Solder

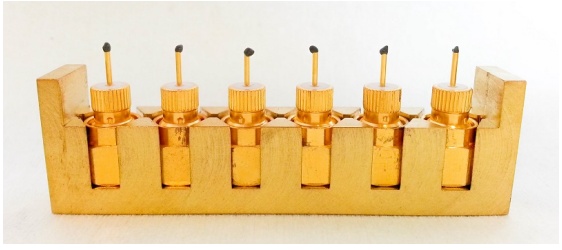

FIGURE 3.5: Prepared SMA connectors (high frequency filters) for insertion

Mark enclosures with a metal stamp to indicate assembly date and creator. Before beginning, solvent clean (Acetone, IPA) the enclosure (A). Screw on an SMA cap (C) for each knurl connector (D), insert them into the insertion aligner (B), and put a dab of solder paste (I) on the pin as shown in Figure 3.5. SMA caps (C) are much cheaper than properly terminated end caps. These caps will get dirty in step 3 so avoid using 50 Ω terminated caps. Check with a caliper that the opening of the cavity (A) for inserting connectors (D) is close to 200 mils in diameter. Any smaller will make inserting connectors difficult and could break the connectors. Any larger will compromise durability and cause a leak.

Insert connectors (D) into the enclosure (A) one side at a time. For enclosures that have two layers (A*), insert connectors into one side of both layers before inserting connectors into the other side. This will ensure that there is always an even surface to push against to prevent angular insertion error.

(A) Press fitting first side

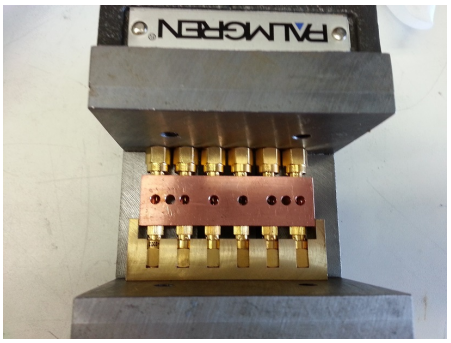

(B) Press fitting second side

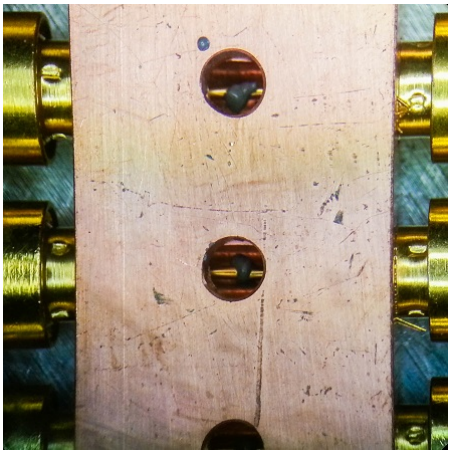

(C) Before soldering

(D) After soldering

FIGURE 3.6: Step 1

Align the insertion assembly (B+C+D) with the enclosure (A), making sure that the knurl part of the connector is snug against the opening of the cavity. Use a clamp to push the connectors (D) into the enclosure (A) as shown in Figure 3.6a. A bit of force is required and the connectors (D) will not go all the way in. When the connectors (D) are about halfway in, we can push two connectors (D) in at a time. Pull off the insertion aligner (B) and screw off the middle four caps (C). Use the clamp to push the outer two connectors (D) in until the connector catches onto the counterbore (when knurl of the connector is completely inside). Move the two caps (C) inward and repeat until all connectors (D) are properly inserted. Screw back on the caps (C). If the enclosure is dual layered, repeat the insertion process on the **same side**. Repeat the insertion process for the other side as shown in Figure 3.6b.

The pins of both connectors from the opposite side should look like Figure 3.6c through the injection hole. The pins should be coaxial for best reflection performance. Use a

soldering iron with a slightly dull tip so that the tip touches at the two pin ends and the solder paste. Insert the soldering iron into the injection hole and lever the tip against the soldering joint, holding for around 5 seconds. In most cases, the solder job will be good as shown in Figure 3.6d without having to look into the cavity while soldering. Solder paste can always be added through the injection hole if needed. After soldering, use a multimeter to check for connectivity and shorts to ground. The enclosure is now ready for ECCOSORB injection.

3.3.2 Step 2: ECCOSORB Preparation

Recommended Frequency and Mixing Ratios by Weight

Series	Range (GHz)	Part X	Part Y
CR-110	26+	100	12.0
CR-112	12 - 18	100	8.2
CR-114	10 - 14	100	4.8
CR-116	6 - 12	100	3.0
CR-117	4 - 8	100	2.3
CR-124	5 and below	100	2.0

Use for high frequency filter — Use for low frequency filter

Recommended Cure Schedule

Temperature	Cure Time
165°F (74°C)	12 hours
200°F (93°C)	4 hours
250°F (121°C)	2 hours
300°F (149°C)	1 hour

(A) http://www.eccosorb.com/Collateral/Documents/English-US/CR.pdf

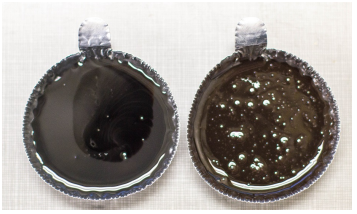

(B) Left: CR-110 Unmixed, Right: CR-110 Mixed, before out gassing

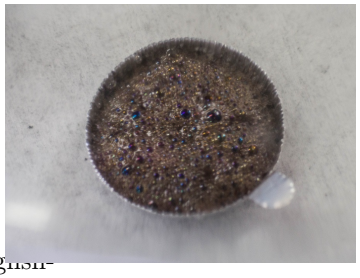

(C) CR-110 Out gassing in vacuum

FIGURE 3.7: Step 2

Weigh out the appropriate proportions of part X (EX) and part Y (EY) in a tray (F) according to the first table above (Figure 3.7a). CR-124 is much more viscous than CR-110, so preheating will help with workability. The recommended preheating temperature is 65° C. Although higher temperatures (150° C) will make the mixture much easier to work with, there will be a shorter window of usability before it starts curing. After preheating and preparing a homogeneous mixture of parts X (EX) and Y (EY) (Figure 3.7b) (using e.g. a stick (G)), place the mixture in a vacuum chamber for 5 minutes to prevent out gassing during the curing process (Figure 6c). If needed, reheat the mixture to recover fluidity.

3.3.3 Step 3: Injection and Curing

Preheat the prepared enclosure (A) from step 1. Use a glass pipette (H) to inject the mixture into the enclosure cavity. Air bubbles may become trapped when injecting into the cavity. Surface tension of the less viscous CR-110 may block the opening to the cavity. Thus, slow and careful injection at a flat angle is needed to prevent this (Figure 3.8a). Use a small wire or sharp object to poke out any air bubbles (Figure 3.8b). For longer cavities, make sure to tilt the enclosure (A) from side to side to ensure that the mixture is filled uniformly inside. Cure according to the second table from step 2. After curing for the appropriate time and letting the filter cool, thermal cycle the filters and check for typical reflection and transmission as shown in the following section. Sand off the oxidized copper to ensure good thermal conductivity in the fridge (Figure 3.8c).

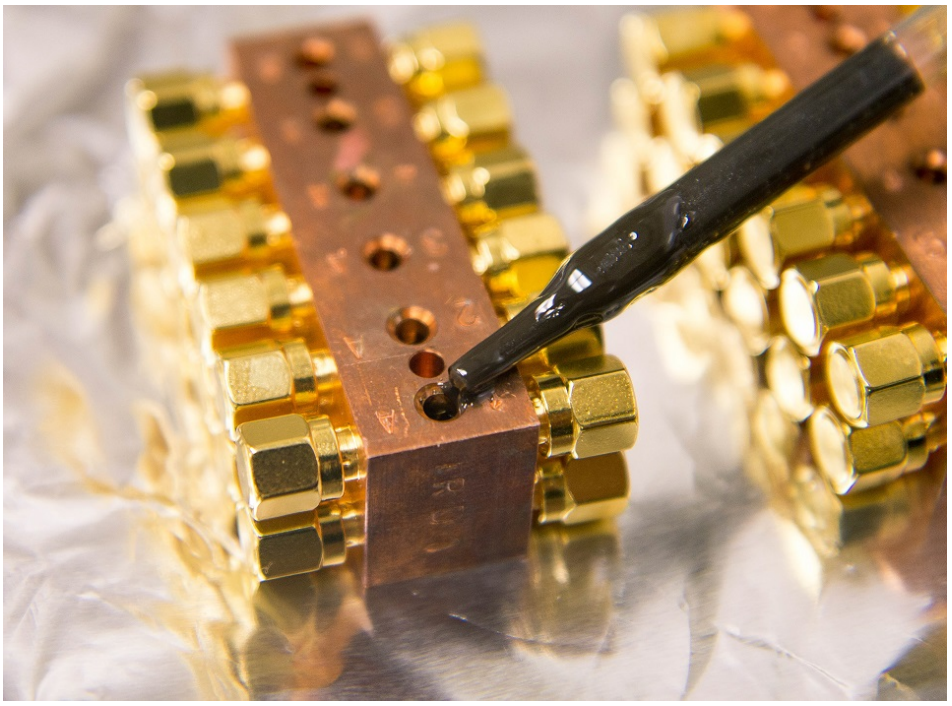

(A) ECCOSORB injection. Inject slowly and at a flat angle such that the liquid creeps onto the edge of the fill opening and into the cavity. Injecting too fast or steep will cause a planar bubble to form which blocks the opening (see Figure 3.8b).

(B) Close up view showing formation of a planar bubble formed from improper injection

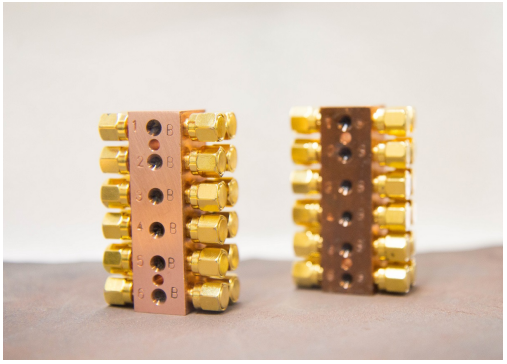

(C) Sand off the accumulated oxide for better thermal conductivity. Left: sanded. Right: not sanded.

FIGURE 3.8: Step 3

3.4 Typical Microwave Characteristics

Before measuring S parameters, filters are thermally cycled. This process is to ensure that the device will not fail from thermal shock. Filters are cooled by being dipped into a bath of LN2 followed by a heating process using a hairdryer. This process is repeated for a total of at least three times so that the device will survive multiple cooldowns. The Agilent PNA-X is used to measure and save S parameters. The PNA-X is always first calibrated to the Electronic Calibration Module N4691B before measuring.

3.4.1 High Frequency Filters

High frequency filters are typically measured to have low reflection (below -25 dB) up to 7.5 GHz and about 0.1 dB/GHz attenuation at 300K as shown in Figure 3.9. Due to the simple press fit assembly and simple transmission line design, these filters will easily exhibit consistently low reflection across a wide operating band. The attenuation given by Emerson and Cumming, about 0.2 dB/GHz attenuation, is stronger perhaps because it assumes a thickness of the dielectric absorber that can be approximated in the infinite thickness limit. In these filters, the dielectric absorber is only 1.2 mm thick.

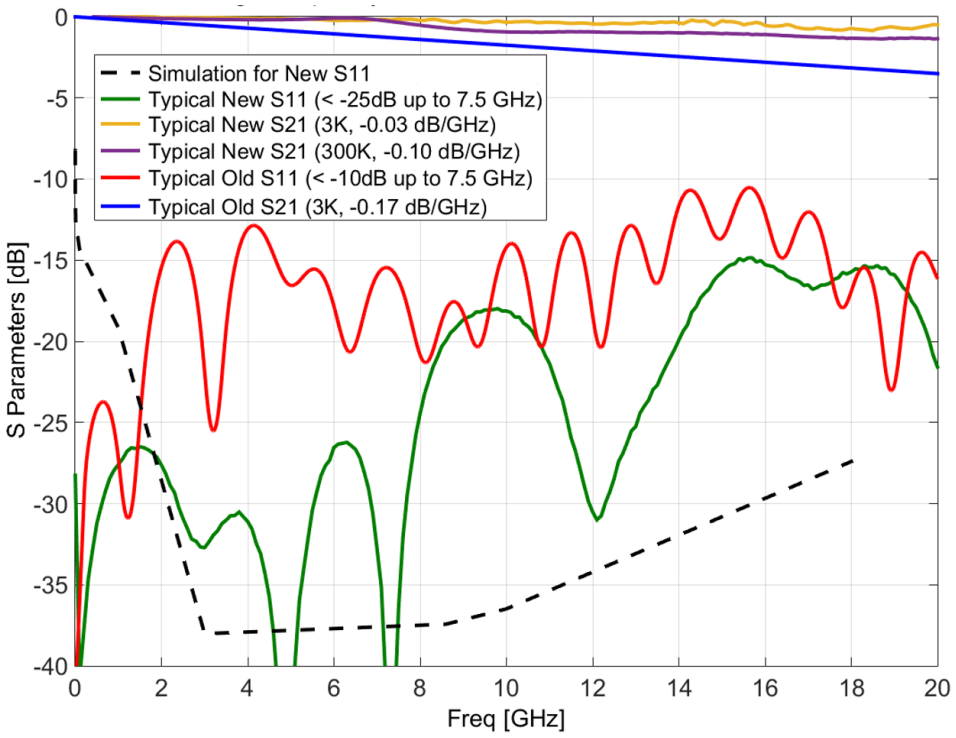

FIGURE 3.9: Typical reflection (300K in green) and transmission (300K in purple, 3K in yellow) for a typical high frequency filter. The previous generation infrared filter has its transmission and reflection at 300K shown in blue and red respectively. The simulation for reflection (dashed black) done in Section 3.1 shows general agreement and predicts a broadband of minimal reflection.

To mitigate the passage of hot electrons into our filter, short Niobium cables are added in series before the filters at the mK stage in the fridge. Since copper and brass are not superconductors, the hot electrons will thermalize much faster through the Niobium cable than through the filter.

3.4.2 Low Frequency Filters

Low frequency filters should have about -20 dB/GHz transmission at 300K as shown in Figure 3.10. Very low reflection is not crucial for low frequencies and is difficult to design for. For an ideally matched coaxial geometry, the outer coaxial diameter would need to be larger than the knurl of the connector. Allowing outer conductor diameter to be smaller fixes this issue as a trade off between reliability and reflectivity. Despite the impedance mismatch, these ECCOSORB filters provide lower reflection than filters with wound wires in a copper powder and epoxy mixture filling. In some cases, as seen

in copper powder filters, too much reflection can cause unwanted standing waves in the fridge wiring.

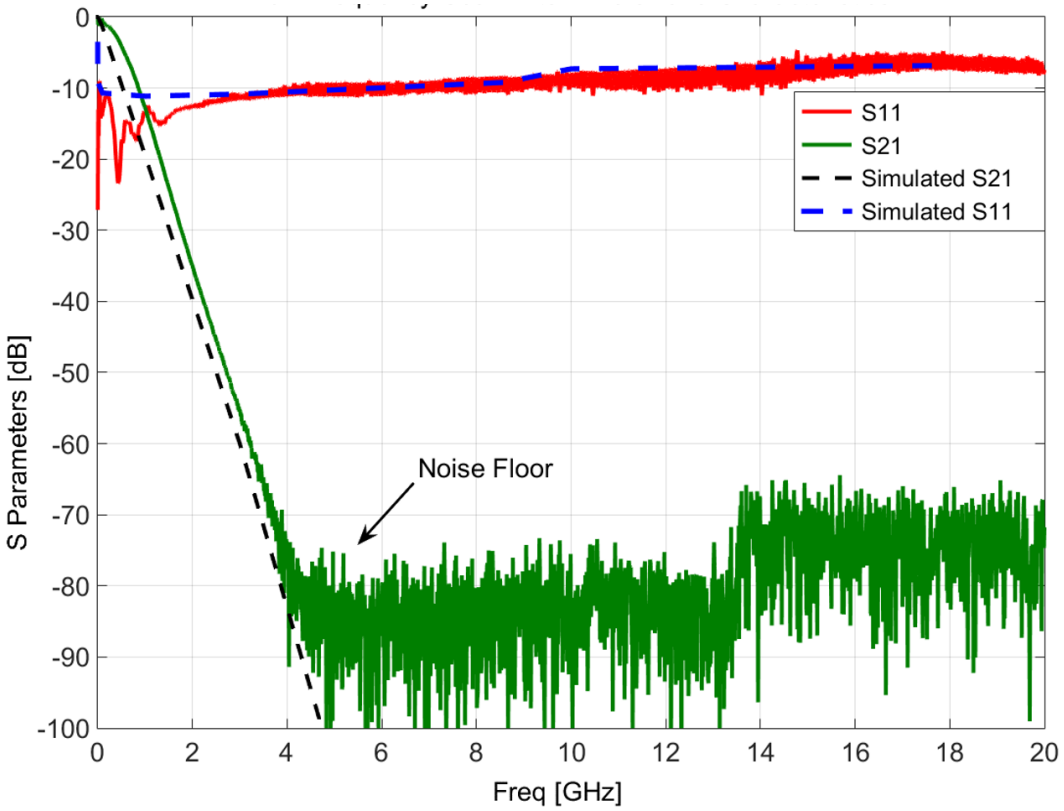

FIGURE 3.10: Typical attenuation (green) and reflection (red) of low frequency filters. The simulation from Section 3.1 shows a very prediction for both attenuation (dashed black) and reflection (dashed blue). The jump in noise floor at 13.5 GHz is caused from a mode switch in the network analyzer.

A variation of the low frequency filter is the port incorporated filter, which allows DC lines to be filtered at the port of mix plate instead of wiring to a filter mounted on the mix plate. This considerably reduces experimental real estate, leaving more room for qubit boxes and wiring. These filters come in two pieces and have a total of 22 lines when put together. The assembly of this filter is the same as covered above with a couple of exceptions.

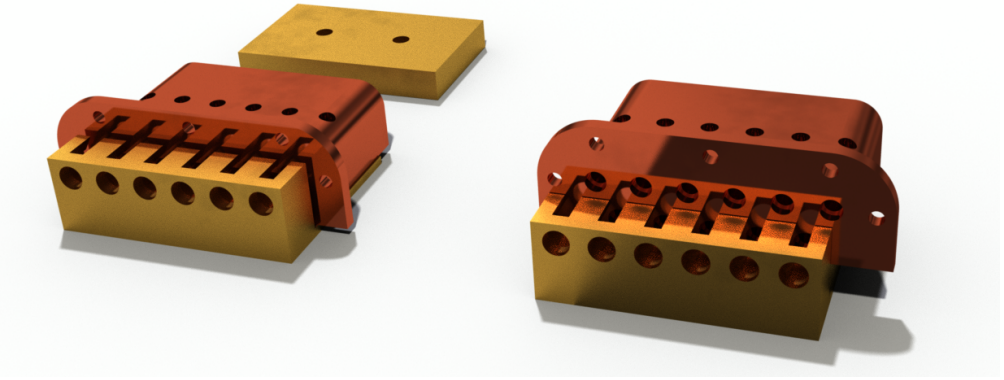

FIGURE 3.11: Left: A special aligner is used with this filter to fill the top layer of connectors, which is done first. The step up block (placed in the back), is not used at this time. Right: After filling the top row, the step up block is attached to fill the bottom row.

The first exception is how the connector is inserted into the enclosure. A special aligner was made to such that connectors can be inserted at both levels of the filter. The bottom level is defined to be on the flat side of the filter where the two parts mate. Figure 3.11 shows the filter with the aligner in two operating modes. First, use the aligner without a step up block. This allows connectors to be inserted on the top level of the filter. Following the connector filling principle from before, do not start filling up the other side until the current side is filled. To fill the bottom level, attach the step up block which will move the insertion level from the top level to the bottom level.

The second exception is how to cure the enclosure. A block is needed to help thermalize the filter when filling into the cavities on the bottom level. Since this filter has a flange, the surface area for thermalization with the hot place during curing it greatly reduced. Use a copper block to level off the top side of the filter, increasing the surface area. Make sure to sand all interfaces for best thermal conduction.

Chapter 4

Experiment: Classical Correspondence of a Spin 3/2 Kicked Top

In this experiment, three qubits are subjected to a kicked top Hamiltonian. All qubits are evolved identically, thereby constituting a spin 3/2 system. The kicked top model is built up from a linear term, governing qubit rotations on the Bloch sphere, and a non-linear term governing coupling between adjacent qubits. We expect the dynamics of our system, by the principles of quantum mechanics, to not be chaotic i.e. two closely separated initial points on the surface of the Bloch sphere will remain close throughout all time. The classical limit of the kicked top is also analyzed to determine if reasonable correspondence exists between a classical system and one deep in the quantum regime. Such a correspondence is interesting because the classical system exhibits chaotic nondeterministic motion in contrast to a quantum mechanically deterministic evolution. The Lyapunov characteristic exponent (LCE) and the entanglement entropy (S) are used as the basis for correspondence. LCEs characterize the exponential rate of divergence between two initial points and thus gives us a measure of chaoticity, while entanglement entropy measures the entanglement between a subsystem and its complete system.

4.1 Qubit Architecture

The qubit architecture for this experiment comprises of three transmon qubits [9] and three flux bais tunable couplers [10] between every qubit as shown in Fig. 4.1. The

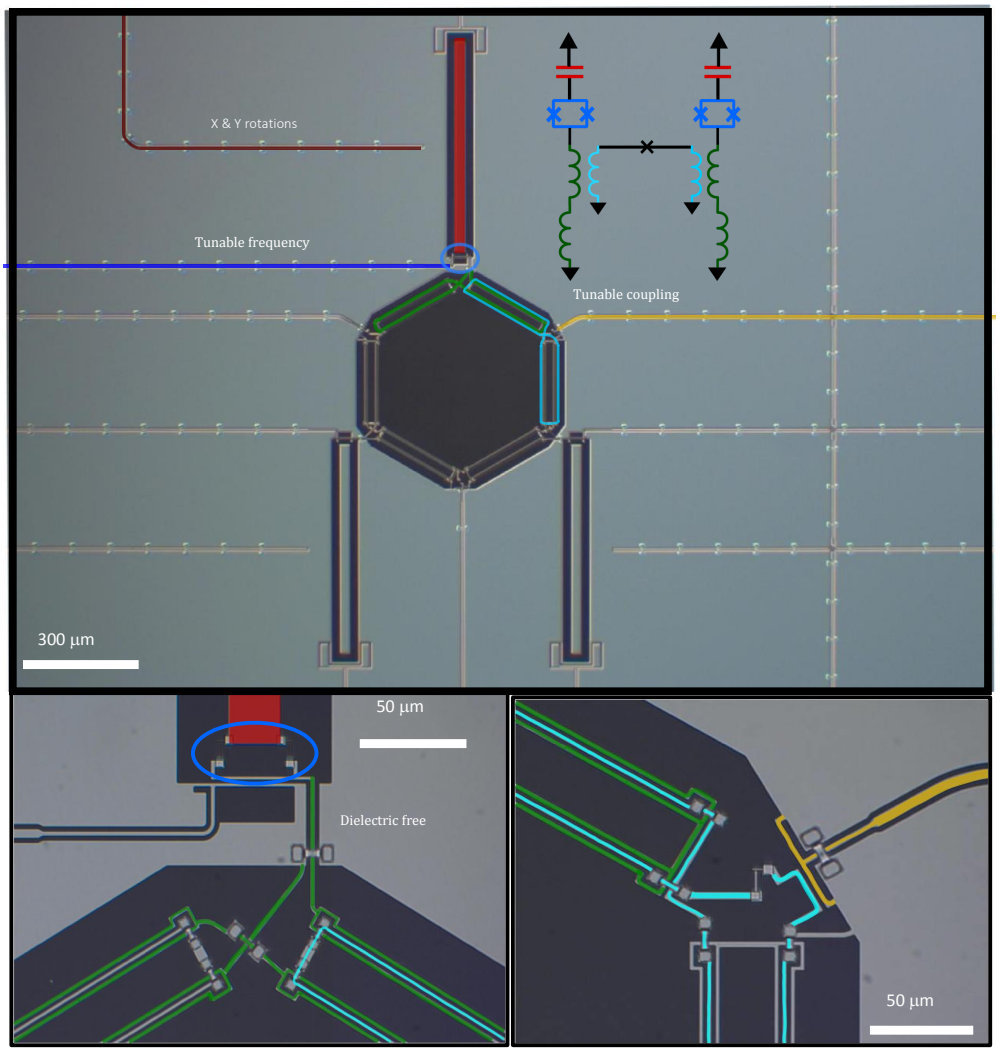

FIGURE 4.1: Three transmon qubits (long red rectangle for capacitor and small blue circle for SQUID loop) fully connected via tunable couples. The tunable coupler is an RF SQUID that is biased with a flux line (yellow). The circuit diagram shown is the coupling scheme between two adjacent qubits, which can be extended to a ring of qubits. The coupler bias loop is galvanically isolated from the qubit circuit to prevent ground loops which will occur from the triangular geometry of the circuit. Mutually coupled waveguides with high inductance on the flux bias loop (cyan) and the qubit path (green) to ground mediate the coupling between two qubits. Figure credit: C. Neill

qubit Hamiltonian in the rotating frame (as shown in Appendix C) with $\Delta_i = \omega_i - \omega_r$, coupling energy g, and the shorthand notation $\sigma_1^x \otimes I_2 \otimes I_3 = \sigma_1^x$ or $I_1 \otimes \sigma_2^y \otimes \sigma_3^y = \sigma_2^y \sigma_3^y$

is

$$H_{3q} = \frac{\hbar}{2}\Bigg[\sum_{i=1,2,3} X_i\sigma_i^x + \sum_{i=1,2,3} Y_i\sigma_i^y - \sum_{i=1,2,3}\frac{\Delta_i}{2}\sigma_i^z + g_{12}\left(\sigma_1^x\sigma_2^x + \sigma_1^y\sigma_2^y\right) + g_{23}\left(\sigma_2^x\sigma_3^x + \sigma_2^y\sigma_3^y\right) + g_{13}\left(\sigma_1^x\sigma_3^x + \sigma_1^y\sigma_3^y\right)\Bigg] \tag{4.1}$$

where g_{ij} is the coupling strength between qubits i and j in rad/s.

Identical y rotations on all qubits allow Y_i to become a single $\theta(t)$. Similarly, g_{ij} becomes a single $g(t)$ coupling term that is also identical for every pair of qubits. By keeping only the relevant terms for the kicked top, σ^y and coupling $\sigma^x\sigma^x + \sigma^y\sigma^y$, we can write a simplified Hamiltonian in terms of the total angular momentum

$$H = \theta(t)\hat{J}_y + g(t)\left(\hat{J}_x^2 + \hat{J}_y^2\right) \tag{4.2}$$

where $\theta(t)$ is a controllable time dependent term for rotations to all qubits about the y-axis on the Bloch sphere and $g(t)$ is a controllable time dependent coupling term between every qubit pair.

4.2 Quantum Kicked Top

The Hamiltonian for the quantum kicked top is

$$H(t) = \frac{\hbar p}{\tau}\hat{J}_y + \frac{\hbar\kappa}{2J}\hat{J}_z^2\sum_{n=-\infty}^{+\infty}\delta(t-\tau n) \tag{4.3}$$

where $\hat{J}_y$ corresponds to a rotation around the y-axis on the Bloch sphere (Figure 4.2) by an angle p and $\hat{J}_z^2$ corresponds to a non-linear, z dependent twist around the z-axis with strength κ. The evolution with this Hamiltonian for one period τ can be written as an unitary operator

$$\hat{U} = e^{-ip\hat{J}_y}e^{-i\frac{\kappa}{2J}\hat{J}_z^2} \tag{4.4}$$

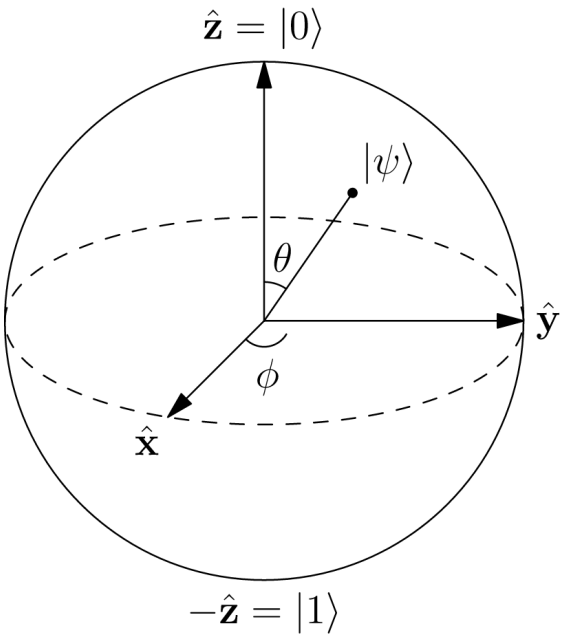

FIGURE 4.2: Bloch sphere representation of a single qubit state. $|0\rangle$ represents the ground state and $|1\rangle$ represents the first excited state. Rotations around the z axis are rotations in phase. Rotations around x and y can have two effects: 1. modulate probabilities between $|0\rangle$ and $|1\rangle$ 2. modulate the phase of the qubit state.

as shown in Appendix B. The system is initialized by setting all three qubits into the same initial state, where a single qubit state is

$$|\psi_0\rangle = |\theta_0, \phi_0\rangle = \cos(\theta_0)\,|0\rangle + e^{-i\phi_0}\sin(\theta_0)\,|1\rangle \tag{4.5}$$

which can be represented on the surface of a unit sphere as shown in Figure 4.2. The full qubit state $|\theta_0, \phi_0\rangle \otimes |\theta_0, \phi_0\rangle \otimes |\theta_0, \phi_0\rangle$ is stroboscopically evolved using Eq. 4.4.

4.2.1 Experimental Implementation

In order to evolve our three qubit system with the kicked top Hamiltonian, we must map the kicked top Hamiltonian to our qubit Hamiltonian. We can then discretize our Hamiltonian (Appendix B) for our microwave pulses on our DAC microwave control boards.

The $\hat{J}_y$ term in the Hamiltonian is simply a y rotation of the state on the Bloch sphere. The $\hat{J}_z^2$ term can be mapped to the coupling term of the qubit Hamiltonian, $\hat{J}_x^2 + \hat{J}_y^2$ since $\hat{J}^2 = \hat{J}_x^2 + \hat{J}_y^2 + \hat{J}_z^2$. The fact that an identity term only contributes a phase to

your state vector (Appendix E) allows us to transform our qubit Hamiltonian into

$$\hat{H} = \theta(t)\hat{J}_y + g(t)\left(J^2\hat{I} - \hat{J}_z^2\right) = \theta(t)\hat{J}_y - g(t)\hat{J}_z^2. \tag{4.6}$$

Comparing this to 4.3, we can see that there is only a sign difference on the non-linear term. This sign difference produces identical phase space dynamics that is equivalent to reflecting about the ϕ axis. The time dependent θ term is implemented experimentally by using pulses which apply rotations to the state of the qubit on the Bloch sphere by an angle $p = \frac{\pi}{2}$. The pulse is a sine wave shaped with a Gaussian envelope such that the integration from the beginning to the end of the pulse gives an accumulated phase of $\frac{\pi}{2}$ in the y quadrature. The computer generated pulse is sent from a DAC board, through cryogenic cabling and filters, to the XY line to manipulate the qubit (shown in red in Figure 4.1) with rotations around the x and y axis on the Bloch sphere. The time dependent coupling term g corresponding to κ is controlled with the tunable coupler via a flux bias. The coupler is characterized by measuring flux bias vs the qubit SWAP rate. Once the coupling strength and flux bias relation is known, any time dependent interaction can be implemented through flux control. In the case of the kicked top, all qubits initially begin in the ground state. Rotations are applied to each qubit to set the initial state $|\theta_0, \phi_0\rangle$. For each "kick," all qubits receive a $\frac{\pi}{2}$ pulse for p, are set to their resonant frequency, and are subjected to a fixed κ dependent coupling.

4.2.2 Entanglement Entropy

Entanglement entropy gives a measure of the accessibility of phase space due to entanglement and is defined as

$$S = -\mathrm{Tr}\rho_{q1}\log_2(\rho_{q1}) \tag{4.7}$$

where ρ is the traced out density matrix for a single qubit, $q1$. We use $\log_2$ so that the dimension of the Hilbert Space, $d = 8$ gives an maximum S of 3, or for a single qubit S of 1. The time average of entanglement entropy $\langle S \rangle$ is interesting because it characterizes the long term behavior of S which is periodic in time. Figure 4.3 with $\kappa = 0.5$ and 2.5

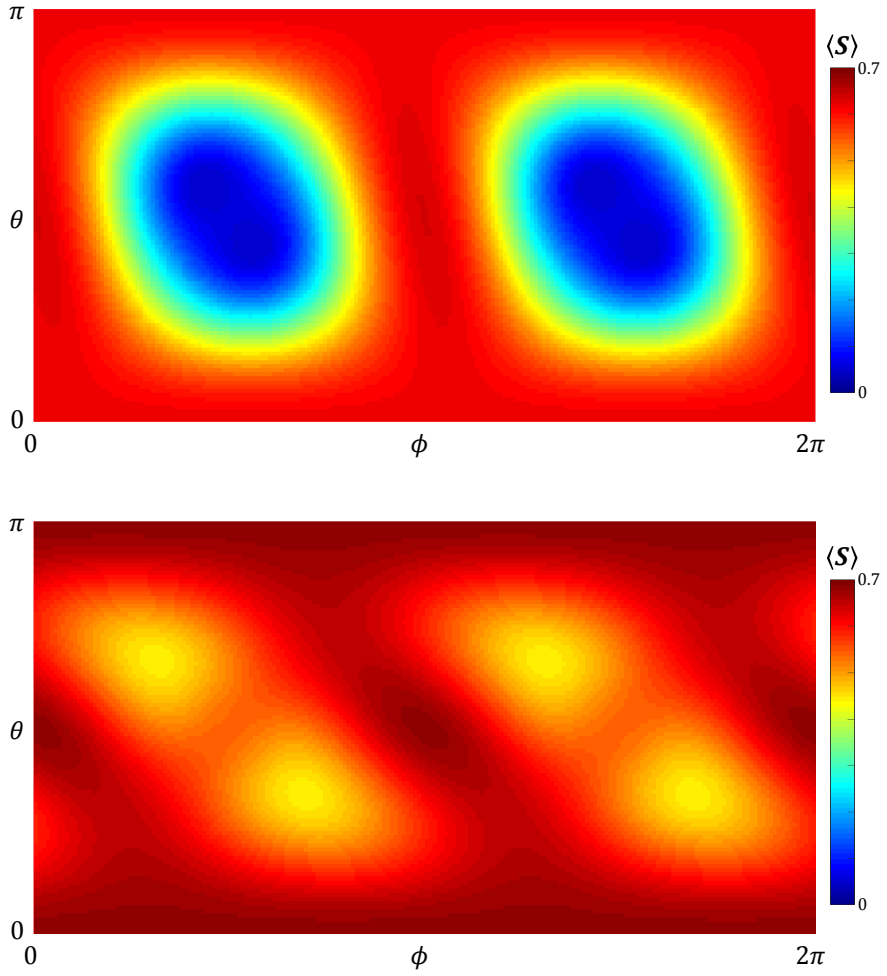

FIGURE 4.3: Entanglement entropy time averaged over 100 kicks of initial points in the Bloch sphere phase space. $p = \frac{\pi}{2}$ and (Top) $\kappa = 0.5$ (Bottom) $\kappa = 2.5$.

shows that the non-linear κ term influences the phase space diagram and the minimum entanglement entropy.

4.3 Classical Kicked Top

When taking $J \to \infty$, the Hamiltonian for the classical kicked top becomes

$$H(t) = pJ_y + \kappa J_z^2 \sum_{n=-\infty}^{+\infty} \delta(t-n) \tag{4.8}$$

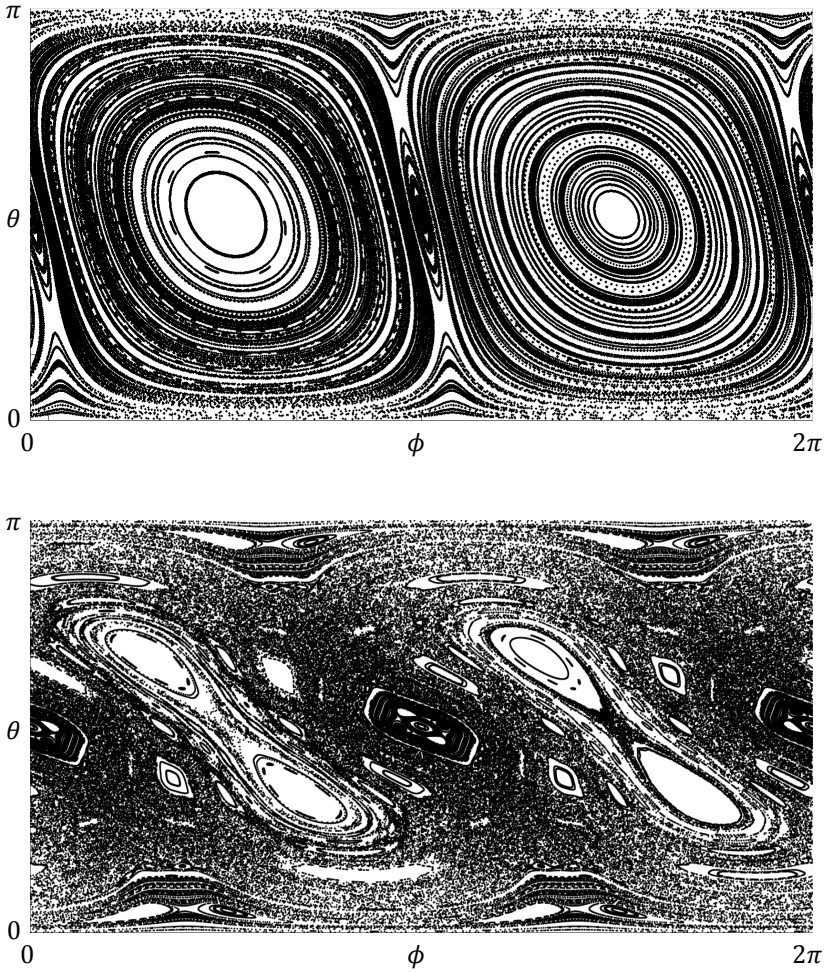

FIGURE 4.4: Classical trajectory of random initial points in the Bloch sphere phase space for $p = \frac{\pi}{2}$ and (Above) $\kappa = 0.5$ (Below) $\kappa = 2.5$.

and can be written as discrete map on the unit sphere. The mapping is a rotation around the y axis by an angle p followed by a nonlinear rotation around the z axis [11]

$$\vec{L}_{n+1} = R_z(\kappa L_z) R_y(p) \vec{L}_n \tag{4.9}$$

where $L_z = \cos(\theta_n)$ is the projection of the current position on the unit sphere projected onto the z axis. The classical stroboscopic phase space trajectories are plotted for a set of random initial points in Figure 4.4. Trajectories for $\kappa = 0.5$ show clear and stable orbits. There is no clear indication of chaotic movement at low values of κ. At $\kappa = 2.5$, chaos appears as a noisy sea. Regions of stability still exist and are characterized by clean quasi-elliptic orbits.

4.3.1 Lyapunov Exponent

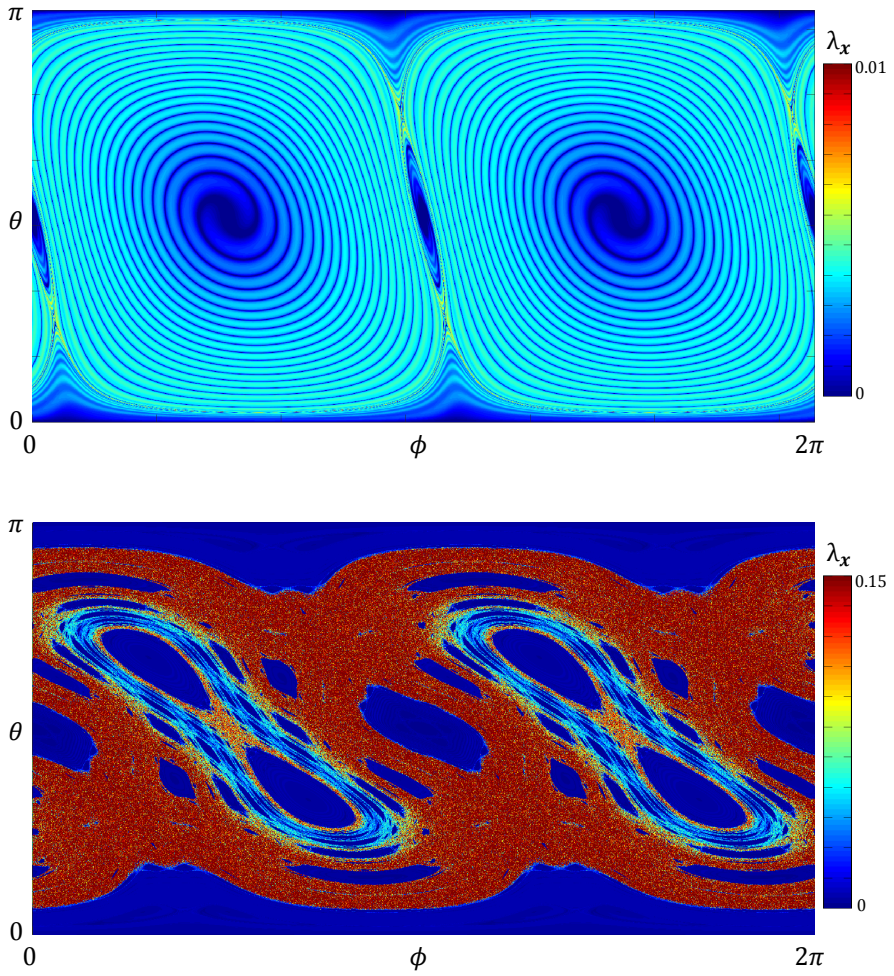

FIGURE 4.5: LCE along the x axis, λ_x, for $p = \frac{\pi}{2}$ and (Above) $\kappa = 0.5$ (Below) $\kappa = 2.5$.

The Lyapunov characteristic exponent (LCE) is a tool used for study the exponential divergence of two closely separated initial points in chaotic dynamical systems. The LCE is defined [12] as

$$\lambda(n) = \lim_{d(0)\to 0} \frac{1}{n} \log\left(\frac{d(n)}{d(0)}\right) \tag{4.10}$$

for the nth kick of the kicked top in Eq. 4.9 as the separation between two initial points goes to zero. LCEs are found numerically as shown in Appendix D. Since our map is of dimension three, we obtain three LCEs for the x, y, and z axes. Our model gives two special properties for the spectrum of LCEs:

- Liouville's theorem for Hamiltonian dynamics restricts the sum of LCEs to be zero
- Conservation of angular momentum restricts one of the LCEs to be zero

We expect $\lambda_y = 0$ to satisfy the second property because the Hamiltonian describes a continuous rotation around the y axis and averages out to zero. The first property leaves us with $\lambda_z = -\lambda_x$. Since λ_x and λ_z have opposite sign and contain redundant information, we use the positive LCE λ_x to describe the chaotic dynamics of our Hamiltonian.

λ_x is plotted in phase space in Figure 4.5 for $\kappa = 0.5$ and 2.5. For $\kappa = 0.5$, λ_x stays below 0.01. Classical phase space (Figure 4.4) shows that all trajectories are in stable orbits. For $\kappa = 2.5$, λ_x rises much above 0.01 for unstable regions and about half of the phase space is characterized by a noisy LCE. When comparing the phase space portrait of LCEs to the time averaged entanglement entropy found in Figure 4.3, we see that all values of $\langle S \rangle$ are stable for $\kappa = 0.5$, where as only the maximum and minimum of $\langle S \rangle$ seem to lie in classically stable regions. This hints at a correspondence between the entanglement entropy and the Lyapunov exponent for each κ where a certain band of $\langle S \rangle$ exhibits classical chaos.

4.4 Correspondence

In the quest to relate quantum and classical measures of disorder, assume that classically chaotic trajectories only occur if $\langle S \rangle$ exists in a certain range e.g. $(\langle S \rangle_{\text{classical min}}, \langle S \rangle_{\text{classical max}})$ at a point (θ, ϕ) in phase space. We define $\langle S \rangle_{\text{classical min}}$ to be the minimum value of $\langle S \rangle$ for the set of points that satisfy $\lambda_x > 0.05$. $\langle S \rangle_{\text{classical max}}$ is the maximum $\langle S \rangle$ for such a set of points. For $0.125 \geq \kappa \geq 3.5$, we plot $\langle S \rangle_{\text{classical min}}$ and $\langle S \rangle_{\text{classical max}}$ along with $\max(\langle S \rangle)$ and $\min(\langle S \rangle)$ in Figure 4.6. For the threshold $\lambda_x > 0.05$, all values of $\langle S \rangle$ correspond to classically stable trajectories until $\kappa = 1.5$. It makes sense to label this region "**Classically Stable**". Beyond $\kappa = 1.5$ a band of minimum and maximum values $(\langle S \rangle_{\text{classical min}}, \langle S \rangle_{\text{classical max}})$ emerges for classically chaotic points. All values of $\langle S \rangle$ outside this band will correspond to classical stable orbits and labeled "**Classically Stable**" and all values of $\langle S \rangle$ inside this band will be labeled "**Classically Chaotic**."

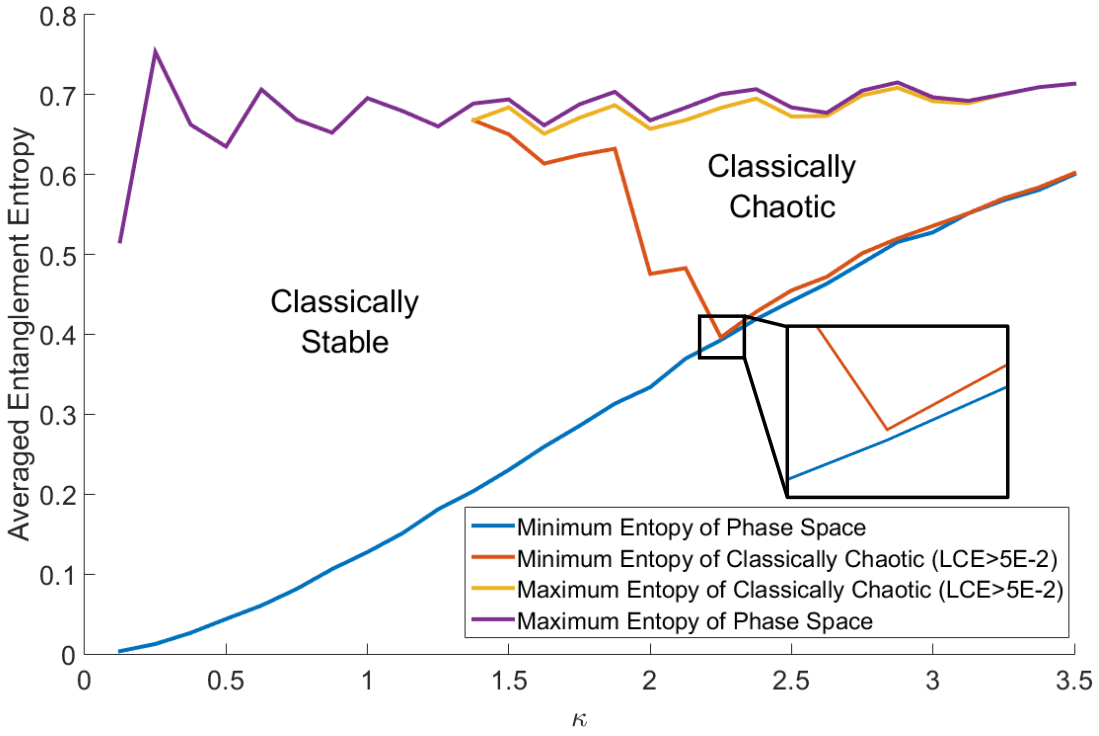

FIGURE 4.6: Allowed values of entanglement entropy corresponding to classically chaotic and stable trajectories. Blue: $\min(\langle S\rangle)$, Orange: $\langle S\rangle_{\text{classical min}}$, Yellow: $\langle S\rangle_{\text{classical max}}$, Purple: $\max(\langle S\rangle)$

There is no guarantee that values of $\langle S\rangle$ within the band will always be classically chaotic. Rather, the band should serve as a rough approximation for the classical dynamics. We can check that values of $\langle S\rangle$ that lie within $(\langle S\rangle_{\text{classical min}}, \langle S\rangle_{\text{classical max}})$ roughly correspond to classically chaotic regions by plotting and comparing to the phase space plot λ_x as shown in Figure 4.7. We see much stronger correspondence, where the classically stable regions are largely outside the band, and classically chaotic regions are largely inside the band. At $\kappa = 1.625$, we have a bound where $\langle S\rangle_{\text{classical min}} = 0.6138$ and $\langle S\rangle_{\text{classical max}} = 0.6511$. The emergence of chaos has just begun and the band is small. Discerning what is chaotic or stable is difficult at this point. At $\kappa = 2.5$, we have a bound where $\langle S\rangle_{\text{classical min}} = 0.4551$ and $\langle S\rangle_{\text{classical max}} = 0.6727$. Chaos is more prominent and areas can be classified as chaotic or stable. However, there are hyperfine regions of stability around the coupled diagonal lobes which characterized with lower values of $\langle S\rangle$. These regions cannot be easily classified as completely chaotic or complete stable. At $\kappa = 3.5$, we have a bound where $\langle S\rangle_{\text{classical min}} = 0.6019$ and $\langle S\rangle_{\text{classical max}} = 0.7137$.

The difference between stability and chaoticity is clear. The band also gives room for small stable regions found at a high κ value.

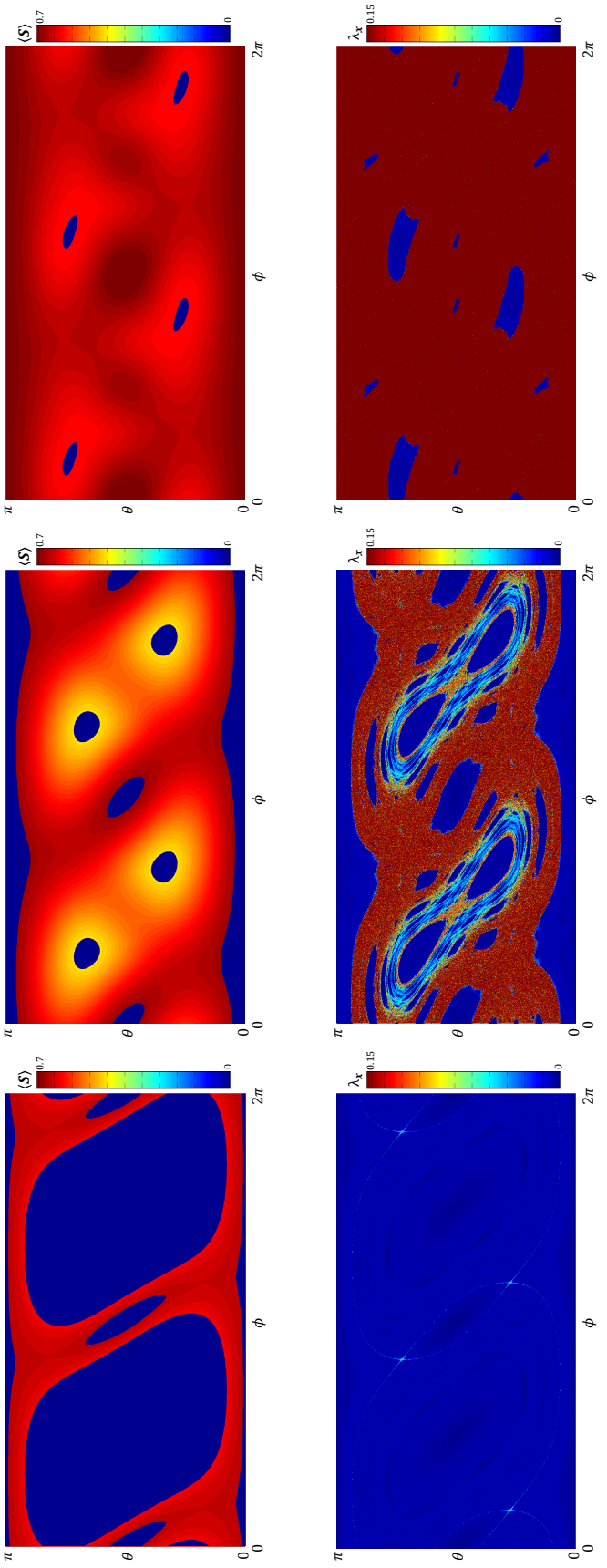

FIGURE 4.7: (Left column) $\kappa = 1.625$. (Middle column) $\kappa = 2.5$. (Right column) $\kappa = 3.5$. We restrict values of $\langle S \rangle$ to $\langle S \rangle_{\text{classical min}}$ and $\langle S \rangle_{\text{classical max}}$ which are extracted from Figure 4.6. We see a better correspondence between the LCE map and the restricted band values of $\langle S \rangle$ when compared to the maps in Figures 4.3 and 4.4.

Chapter 5

Conclusions and Future Prospects

Quantum simulation using superconducting qubits is still in its infancy, but current technology still allows for many interesting applications and flexibility. With proper shielding and control, robust and scalable qubits can be made possible. The development of an efficient mechanism to cool down cryogenic cables will enable large scale quantum computation experiments at lower temperatures. New infrared filters will protect superconducting elements from sources of dissipation, while allowing for more control wiring to manipulate qubits.

Interesting quantum systems can already be studied. However, the number of qubits involved is small. One can find a solution just as fast, if not faster, using a classical computer. At a threshold of 20 - 25 qubits, the advantage of simulating a quantum system of such a size using a classical supercomputer will be eliminated. However, scaling up from a few qubits to tens of qubits is not trivial. There are many engineering challenges and physics obstacles to overcome. Adding control wires to a 2D architecture requires multilayer fabrication or a flip chip design. Increasing coherence times will require better materials and fabrication processes. Fortunately, ongoing work is aiming to solve these problems through academic research and industrial development. Over the next few years, there will be increased effort for a scalable architecture, allowing for simulation of complex quantum systems.

Appendix A

Thermal Conductivities

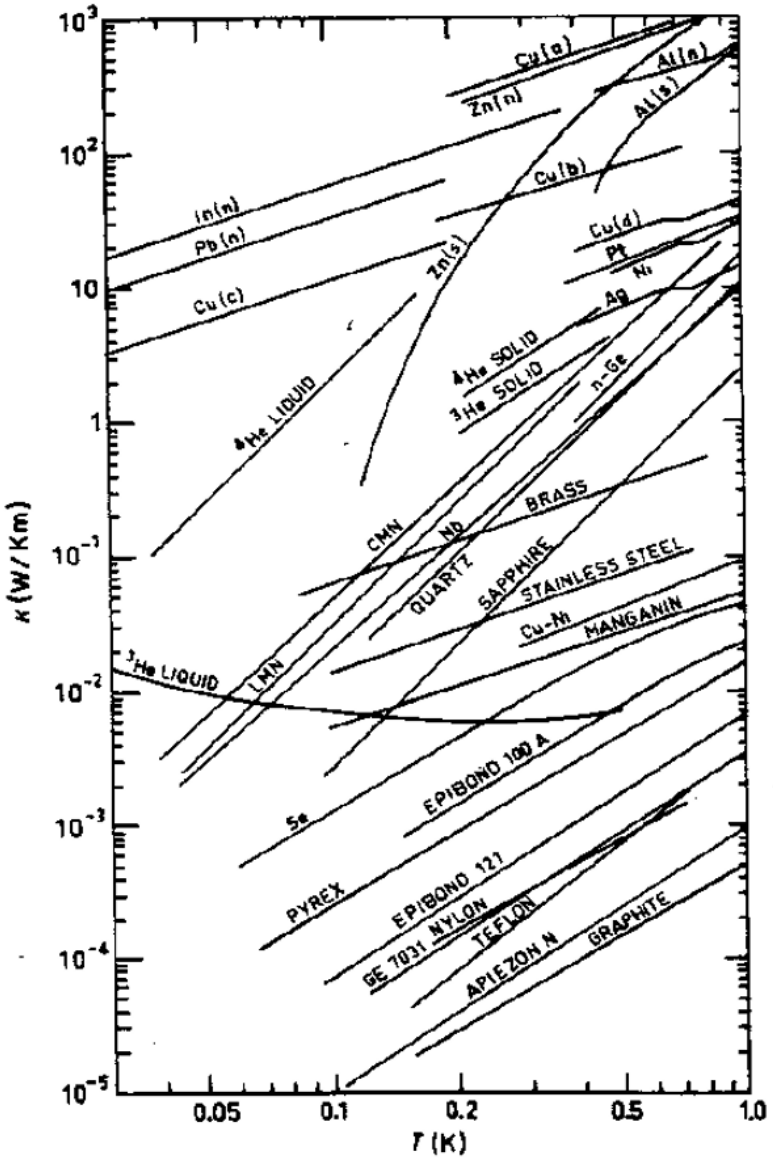

FIGURE A.1: Thermal conductivities for various materials below 1K. This figure is accredited to Lounasmaa.

Appendix B

Floquet Operator and Discretization of the Kicked Top Hamiltonian

To check discretization, we consider Hamiltonian for the quantum kicked top with spin J for kicks of period τ

$$H(t) = \frac{\hbar p}{\tau}\hat{J}_y + \frac{\hbar\kappa}{2J}\hat{J}_z^2 \sum_{n=-\infty}^{+\infty} f(t-\tau n) \tag{B.1}$$

where $f(x) = \delta(x)$, a delta function [1]. We will later approximate the delta function with a normal probability distribution function. We can describe the time evolution by using an operator for each period

$$U(t, t+\tau) = e^{-\frac{i}{\hbar}\int_t^{t+\tau} H(t')dt'}, \quad |\Psi(t+\tau)\rangle = U(t, t+\tau)\,|\Psi(t)\rangle \tag{B.2}$$

since H commutes with itself for all time during each period

$$[H(t_1), H(t_2)] = 0, \text{ with } t_1, t_2 \in [t, t+\tau)\,. \tag{B.3}$$

Since our Hamiltonian is periodic with period τ, the integral term in the exponential can be evenly divided over the total time $t_N = N\tau$, so

$$\int_t^{t+\tau} H(t')dt' = \hbar\left(\int_t^{t+\tau} \frac{p}{\tau}\hat{J}_y + \frac{\kappa}{2J}\hat{J}_z^2 \sum_{n=-\infty}^{+\infty} \delta(t'-\tau n)dt'\right) = \hbar\left(p\hat{J}_y + \frac{\kappa}{2J}\hat{J}_z^2\right) \quad \text{(B.4)}$$

and thus we have the Floquet operator

$$U(t, t+\tau) = e^{-ip\hat{J}_y} e^{-i\frac{\kappa}{2J}\hat{J}_z^2} \quad \text{(B.5)}$$

where taking $m = 0, 1, 2...N$ for $U^m |\Psi(0)\rangle$ would give us a sequence of states from zero to N kicks. Note that the sum for the delta function disappears from the Hamiltonian since we integrated over one period of a cycle. Using this method to time evolve our state is straight forward and allows us to see the stroboscopic evolution of our system.

However, this method prevents us from looking at the dynamics within each period. Instead of integrating the Hamiltonian directly, we can approximate the integral for one cycle from (B.4) by a Riemann Sum ($dt \approx \tau/M$) and replacing the delta function with a periodic normal probability distribution function $g(t)$, with $g(t) = g(t+\tau)$ and $\int_t^{t+\tau} g(t)dt = 1 \Rightarrow \frac{\tau}{M}\sum_{i=1}^{M} g(t_i) \approx 1$with $t_1 = t,\ t_M = t+\tau$ for sufficiently big M:

$$\int_t^{t+\tau} \hat{H}(t')dt' \approx \frac{\tau}{M}\sum_{i=1}^{M} H(t_i'') \text{ with } t_1'' = t,\ t_M'' = t+\tau \quad \text{(B.6)}$$

$$= \hbar\left[\frac{\tau}{M}\sum_{i=1}^{M}\left(\frac{p}{\tau}\hat{J}_y + \frac{\kappa}{2J}\hat{J}_z^2 g(t_i'')\right)\right] \quad \text{(B.7)}$$

$$\approx \hbar\left[\frac{\tau}{M}\left(\frac{M}{\tau}p\hat{J}_y + \frac{M}{\tau}\frac{\kappa}{2J}\hat{J}_z^2\right)\right] \quad \text{(B.8)}$$

$$= \hbar\left[p\hat{J}_y + \frac{\kappa}{2J}\hat{J}_z^2\right] \quad \text{(B.9)}$$

which gives us the same Floquet operator for each kick.

Appendix C

Rotating Wave Approximation

The unitary matrix governing the rotating wave approximation for two qubits is given by:

$$U_{RWA} = \begin{pmatrix} e^{-it\omega_r} & 0 & 0 & 0 \\ 0 & 1 & 0 & 0 \\ 0 & 0 & 1 & 0 \\ 0 & 0 & 0 & e^{it\omega_r} \end{pmatrix}. \tag{C.1}$$

The two qubit Hamiltonian in the spin basis ($|\uparrow\uparrow\rangle, |\uparrow\downarrow\rangle, |\downarrow\uparrow\rangle, |\downarrow\downarrow\rangle$) describing the energies (ω_1, ω_2), applied microwave pulses at frequency ω_r with strength (Ω_1, Ω_2) and phase (ϕ_1, ϕ_2) , and tunable coupling g is given by:

$$H_Q = \hbar \begin{pmatrix} -\frac{\omega_1}{2} - \frac{\omega_2}{2} & \cos(\phi_2 + t\omega_r)\,\Omega_2 & \cos(\phi_1 + t\omega_r)\,\Omega_1 & g \\ \cos(\phi_2 + t\omega_r)\,\Omega_2 & \frac{\omega_2}{2} - \frac{\omega_1}{2} & g & \cos(\phi_1 + t\omega_r)\,\Omega_1 \\ \cos(\phi_1 + t\omega_r)\,\Omega_1 & g & \frac{\omega_1}{2} - \frac{\omega_2}{2} & \cos(\phi_2 + t\omega_r)\,\Omega_2 \\ g & \cos(\phi_1 + t\omega_r)\,\Omega_1 & \cos(\phi_2 + t\omega_r)\,\Omega_2 & \frac{\omega_1}{2} + \frac{\omega_2}{2} \end{pmatrix} \tag{C.2}$$

We apply RWA to our qubit by doing the following [14]:

$$H_{QRWA} = U H_Q U^\dagger - i\hbar U \dot{U}^\dagger \tag{C.3}$$

Let $\Delta_1 = \omega_1 - \omega_r$, $\Delta_2 = \omega_2 - \omega_r$, ignoring the phase and the high frequency $e^{-2it\omega_r}$ terms, we obtain:

$$H_{QRWA} = \hbar \begin{pmatrix} \frac{-\Delta_1-\Delta_2}{2} & \Omega_2 & \Omega_1 & 0 \\ \Omega_2 & \frac{-\Delta_1+\Delta_2}{2} & g & \Omega_1 \\ \Omega_1 & g & \frac{\Delta_1-\Delta_2}{2} & \Omega_2 \\ 0 & \Omega_1 & \Omega_2 & \frac{\Delta_1+\Delta_2}{2} \end{pmatrix} \tag{C.4}$$

Appendix D

Numerical Calculation of the Lyapunov Exponent

Calculating the Lyapunov Characteristic Exponent (LCE) is a numerically demanding task. The following is numerical work originally developed in Mathematica [15].

For a discrete map given by a vector function $\vec{F}$ with $\vec{x}_{k+1} = \vec{F}(\vec{x_k})$, we know that $\vec{x}_k = \vec{F}^k(\vec{x}_0)$. The total derivative at $\vec{x}_k$ given by the chain rule is

$$D_{\vec{x}}\vec{F}^k(\vec{x}_0) = J\left(\vec{F}^{k-1}(\vec{x}_0)\right)\ldots J\left(\vec{F}(\vec{x}_0)\right)J(\vec{x}_0) \tag{D.1}$$

where J is the Jacobian of the vector function $J(\vec{x}_0) = D_{\vec{x}}\vec{F}(\vec{x})\Big|_{x=x_0}$. The first step for finding the LCE is decomposing the Jacobian matrix using QR decomposition, a deconstruction of a matrix into a product of two types matrices: orthogonal (Q) and upper triangular (R). Explicitly, QR decomposition gives us $J(\vec{x}) = Q_1R_1$. If we define for $n = 2, 3, ...k$ that

$$J_n^* = J\left(\vec{F}^{k-1}(\vec{x})\right)Q_{k-1} \tag{D.2}$$

and decompose $J_n^* = Q_nR_n$ for each n, we see from D.1 that $D_{\vec{x}}\vec{F}^k(\vec{x}) = Q_kR_k\ldots R_1$. It is also a consequence that the diagonal elements $P_{ii}^{(k)}$ of the product of upper triangular

matrices $P^{(k)} = R_k \dots R_1$ has the following property:

$$\lim_{k\to\infty} \frac{1}{k} \ln P_{ii}^{(k)} = \lambda_i \tag{D.3}$$

where λ_i is the i-th LCE of the system. So for sufficiently large k, say $k = 1000$, we should obtain the approximate LCE spectrum. We begin this QR decomposition process deep into the evolution of the system, say for a transient $t = 100$, to avoid quasi-stable motion. Thus, the pseudocode for computing the LCE spectrum is as follows:

Data: inital point $\vec{x}_0$, discrete map $\vec{F}(\vec{x})$, Jacobian of discrete map $J(\vec{x})$

Result: LCE spectrum

Initialization: t = 100, k = 1000, LCEs = Zeros(Size($\vec{x}_0$));

for *i = 1, ..., t* **do**

  $\vec{x}_i = \vec{F}(\vec{x}_{i-1})$;

end

temp = $\vec{x}_t$;

[Q,R] = QRdecomposition(J (temp));

for *i = 1, ..., k* **do**

  temp = F (temp);

  [Q,R] = QRdecomposition(J (temp) Q);

  diags = Diagonal(R);

  LCEs = Real(Log(diags)) + LCEs;

end

LCEs = LCEs/k;

Algorithm 1: Computing the LCE spectrum for a discrete map $\vec{F}$.

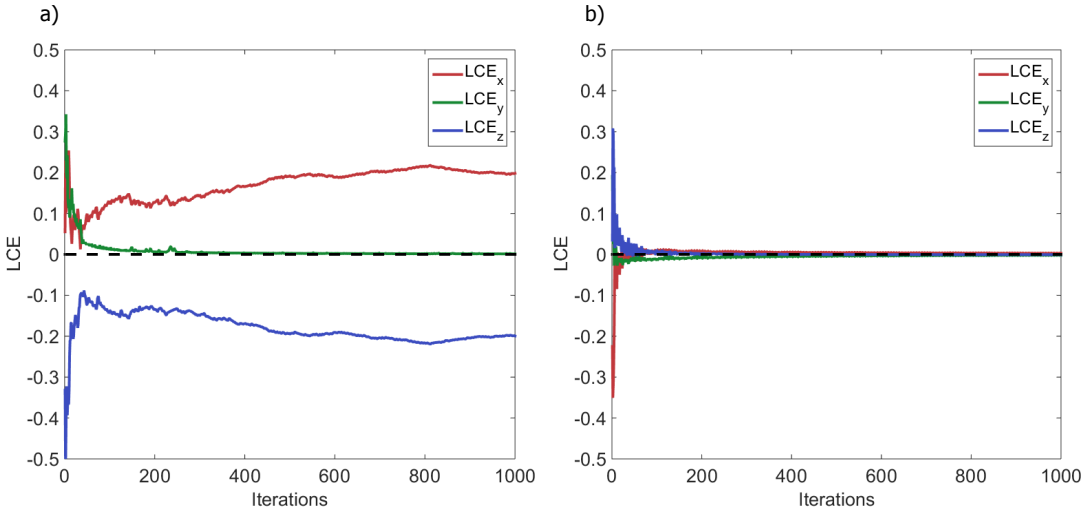

FIGURE D.1: Convergence plot of the LCE spectrum for the classical kicked top using the QR decomposition algorithm outlined above with a transient $t = 100$, iterations $k = 1000$, $p = \frac{\pi}{2}$, and $\kappa = 2.5$. **a)** chaotic initial point $\vec{x}_0 = (\phi_0, \theta_0) = (3, 2)$ **b)** stable initial point $\vec{x}_0 = (\phi_0, \theta_0) = (2, 2)$.

Appendix E

Identity Term in Hamiltonian

Given a Hamiltonian

$$\hat{H} = \hat{H}_0 + \gamma \hat{I} \tag{E.1}$$

where H_0 is some other Hamiltonian and I is the identity with some constant γ. We assume that H commutes with itself for all time. The unitary propagator in differential time is then

$$\begin{aligned}
\hat{U} &= e^{-\frac{i}{\hbar}\hat{H}dt} \\
&= e^{-\frac{i}{\hbar}(H_0+\gamma I dt)} \\
&= e^{-\frac{i}{\hbar}\hat{H}_0 dt} e^{-\frac{i}{\hbar}\gamma \hat{I} dt} \\
&= e^{-\frac{i}{\hbar}\hat{H}_0 dt} \sum_{n=0}^{\infty} \frac{\left(-\frac{i}{\hbar}\gamma \hat{I}\right)^n}{n!} dt \\
&= e^{-\frac{i}{\hbar}\hat{H}_0 dt} \hat{I} \sum_{n=0}^{\infty} \frac{\left(-\frac{i}{\hbar}\gamma dt\right)^n}{n!} \\
&= e^{-\frac{i}{\hbar}\hat{H}_0 dt} \left[\hat{I} e^{-\frac{i}{\hbar}\gamma dt}\right]
\end{aligned}$$

where the first term is an operator and the second term is an identity operator times a constant. Assume after one kick with H_0, we obtain the state $|\Psi\rangle = \begin{pmatrix} a \\ b \end{pmatrix}$. Then with

the full Hamiltonian H we obtain $|\Psi'\rangle = \begin{pmatrix} a \\ b \end{pmatrix} \cdot e^{-\frac{i}{\hbar}\gamma}$, which has an extra global phase factor. We see that the density matrix for the evolution under H is $\rho = |\Psi'\rangle\langle\Psi'| = \begin{pmatrix} a \\ b \end{pmatrix} \begin{pmatrix} a^* & b^* \end{pmatrix} e^{-\frac{i}{\hbar}\gamma} \cdot e^{\frac{i}{\hbar}\gamma} = |\Psi\rangle\langle\Psi|$, which is the density matrix for the state that was evolved under H_0. Since the expectation for an operator A is given by $\langle A\rangle = tr(\rho A)$, the measured outcome is the same.

Appendix F

Classical Effects: Pulse Width and Separation

We study the effects of pulse shape and overlap on the canonical kick top Hamiltonian. In an experimental setting, we might obtain a Hamiltonian which cannot be mapped to a Floquet operator. In this case, we see perturbed trajectories of our classical kicked top and the suppression of chaos. The chaoticity from changing pulse width and separation is characterized and a simple model is proposed to explain how chaoticity changes with pulse shape and separation.

The Hamiltonian of the kicked top includes a periodic δ-function kick or twist of period τ. The Hamiltonian of a kicked top gives chaos through the non-linear term, not the δ-function term. The chaoticity of an initial point in the phase space of a rotator can be characterized by the Lyapunov exponent. Here, the maximal Lyapunov exponent (mLCE) used due to its fast numerical calculation [13]. We can bin chaotic (mLCE > 1) and non-chaotic (mLCE <1) points to measure the population of chaotic initial points. For $p = \pi/4$ and $\kappa = 2.5$, we map chaotic and non-chaotic initial points in phase space. After 500 kicks, most of the chaotic points have saturated to a mLCE > 1 (red) with stable islands with mLCE < 1 (blue) in Figure F.1. Intermediary colors represent the boundary between chaoticity and stability and approximately 44.26% of initial points have chaotic trajectories.

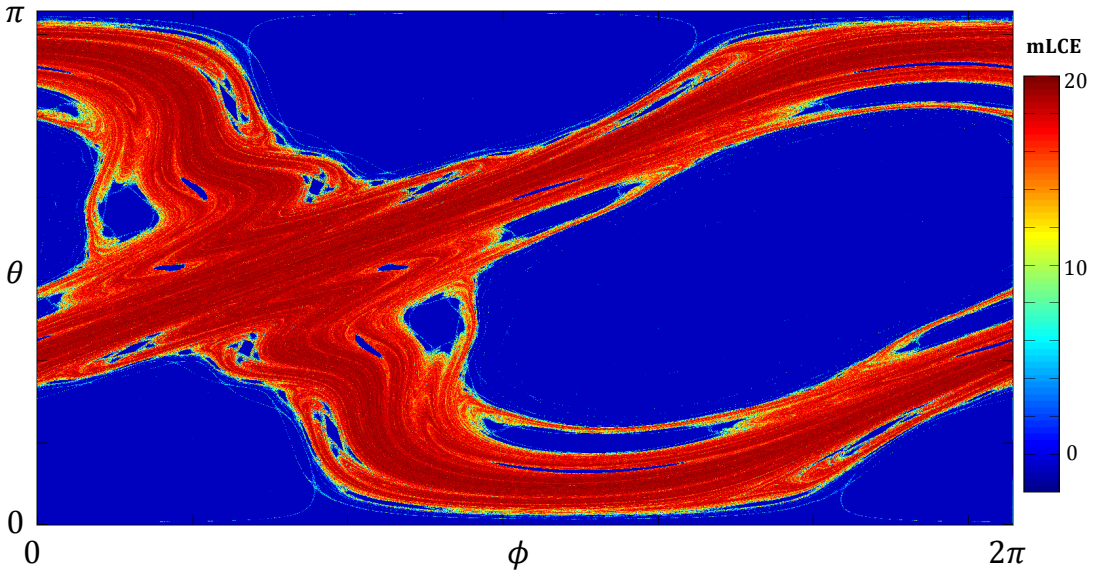

FIGURE F.1: mLCE map for $p = \frac{\pi}{4}$ and $\kappa = 2.5$. Approximately 44.26 % of initial points are chaotic.

The experimental implementation of the quantum kicked top requires two pulses: one for the rotation terms of strength p and one for the twisting term of strength κ. These slides show will that we have great flexibility in choosing pulses to drive our kicked top. The rotating and twisting term over a single kick can be of any shape, given that they do not overlap. The integral of each pulse shape should be equal to the respective kicking or twisting strength. Overlap between the rotating and twisting pulse is avoided to preserve the Hamiltonian. To see the effect of overlapping pulses, Gaussian profiles with uncertainty σ and mean μ are used for linear rotation p and twisting of strength κ

$$f_p(t) = \sum_n \frac{p}{\sigma\sqrt{2}} e^{-\frac{(t-\mu_p - n\tau)^2}{2\sigma^2}} \tag{F.1}$$

$$f_\kappa(t) = \sum_n \frac{\kappa}{\sigma\sqrt{2}} e^{-\frac{(t-\mu_\kappa - n\tau)^2}{2\sigma^2}} \tag{F.2}$$

with a separation between the pulses $\mu_p - \mu_\kappa$ a maximum at $\tau/2$. The "measurement" occurs at the end of every period τ. The two pulses are initially kept maximally separated at $\tau/4$ and $3\tau/4$ for maximum separation to characterize wider Gaussian profiles.

F.1 Pulse Width

At maximum separation, $\tau/2$, the pulse width is widened from $\sigma = 1/8$ to $\sigma = 2/5$ in Figure F.2. The mLCE phase space plot shows that the percentage of chaoticity fades. However, it is still unclear whether this is due the width of the pulses themselves or the overlap between the two pulses.

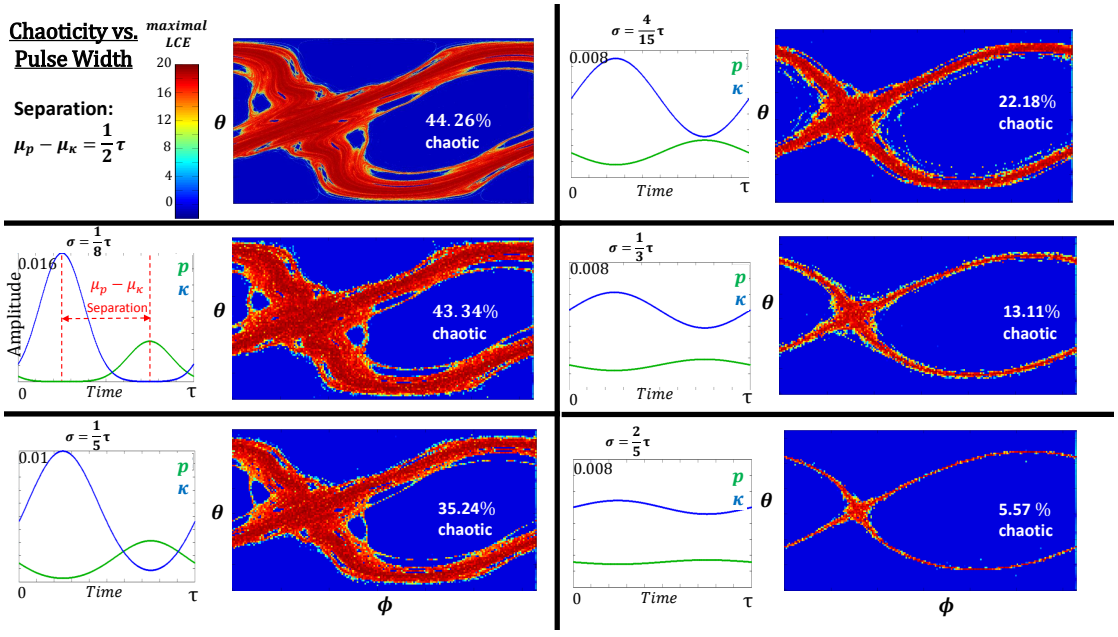

FIGURE F.2: The width of the two pulses are made larger, thereby creating more overlap and perturbations in the Hamiltonian. Such a perturbation partially removes the chaotic dynamics of the system. The parameters used are $p = \frac{\pi}{4}$ and $\kappa = 2.5$.

F.2 Separation

To test another cause for the disappearance of chaos, the pulse width is now held at $\sigma = 1/8$ while the two pulses are brought closer together from maximum separation $\tau/2$ to zero separation in Figure F.3. Again, we see the disappearance of chaos. Chaos disappears nearly completely with zero separation. This hints that the disappearance of chaos is caused by how the two pulses overlap.

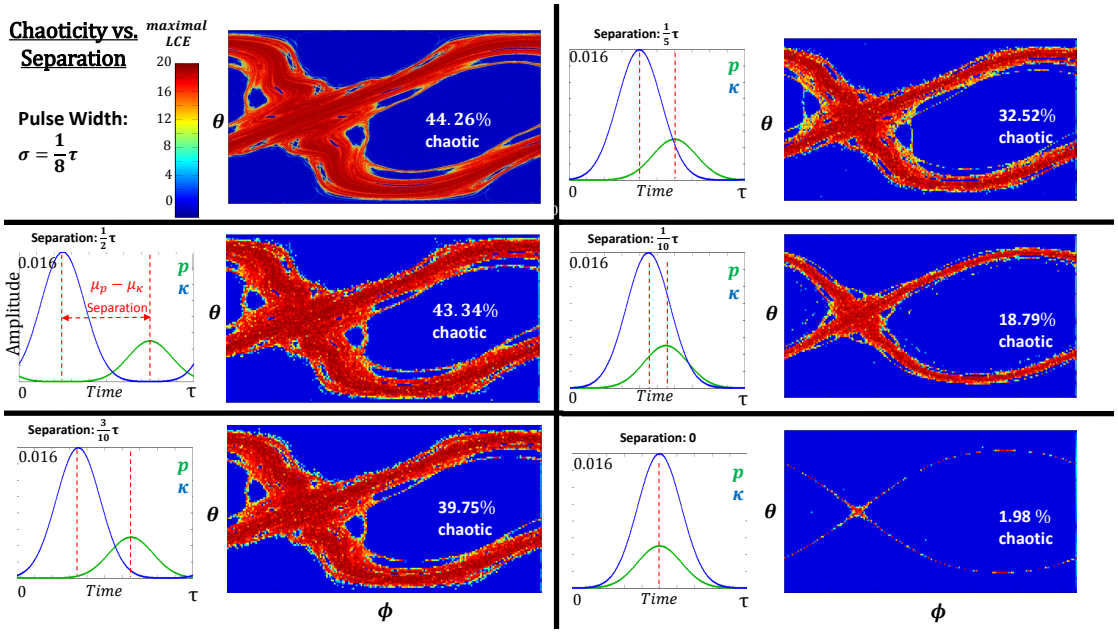

FIGURE F.3: The separation of the two pulses are made smaller, thereby creating more overlap and perturbations in the Hamiltonian. Such a perturbation partially removes the chaotic dynamics of the system. The parameters used are $p = \frac{\pi}{4}$ and $\kappa = 2.5$.

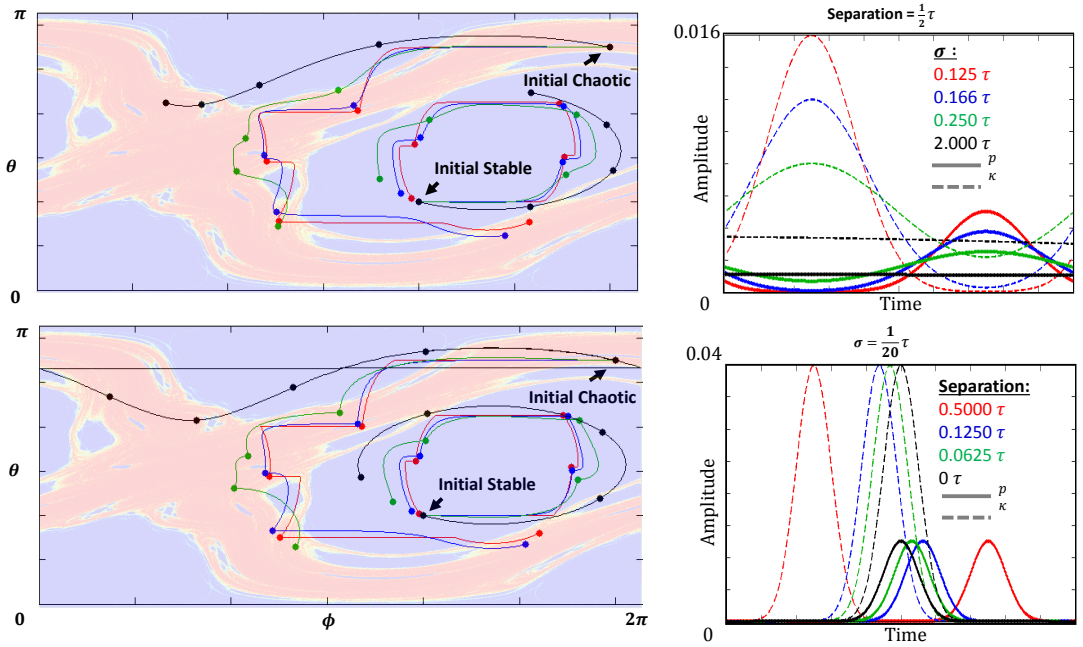

FIGURE F.4: Trajectories of the classical kicked top as (above) pulse width is made larger and (below) separation is made smaller. Both perturbations alter and smooth out stable and chaotic trajectories. The parameters used are $p = \frac{\pi}{4}$ and $\kappa = 2.5$.

F.3 Trajectories

The implementation of wide Gassuian pulses also allows us to follow the trajectories over a continuous time, shown in Figure F.4. Note that the filled circular markers indicate a "measurement" which happens at every kicking period τ. For properly narrow pulses with enough separation to prevent overlap, chaotic initial points stay in the chaotic sea white stable initial points remain in stable orbits. The trajectories themselves can leave their chaotic or stable territories since the actual measured location in phase space is what should remain chaotic or stable. When the pulses are made wider or brought closer together, the measured locations wander into forbidden territory. We also see that changing the pulse width has a different effect on the perturbation in the trajectory than changing the separation.

F.4 Modeling the Disappearance of Chaos

An attempt at modeling the disappearance of chaoticity is defining a measure called the Normalized Integral Difference (NID). NID is defined independently of the kicking strengths, p and κ:

$$NID = \mathbf{max}\left(\int \kappa(t) - p(t)dt\right) - \mathbf{min}\left(\int \kappa(t) - p(t)dt\right) \tag{F.3}$$

where $p(t)$ and $\kappa(t)$ correspond to Gaussian pulses without a scaling factor

$$f_p(t) = \sum_n \frac{1}{\sigma\sqrt{2}} e^{-\frac{(t-\mu_p-n\tau)^2}{2\sigma^2}} \tag{F.4}$$

$$f_\kappa(t) = \sum_n \frac{1}{\sigma\sqrt{2}} e^{-\frac{(t-\mu_\kappa-n\tau)^2}{2\sigma^2}} \tag{F.5}$$

The NID definition is shown graphically in Figure F.5.

The NID is scaled with the chaotic percentage without perturbations and plotted in Figure F.6 against mLCE chaoticity percentages as shown in Figure F.2 and F.3. We see a consistency in behavior between the mLCE data and the scaled NID with slight deviations which seem like constant addition factors. Despite the deviations from the

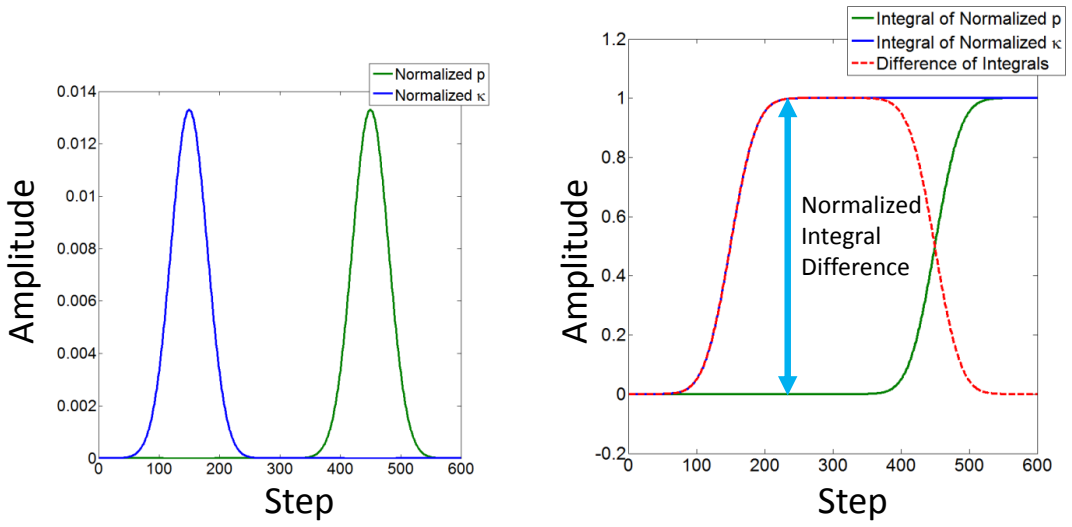

FIGURE F.5: (Left) Normalized pulses corresponding to p in green and κ in blue. (Right) Integrated pulses of p in green and κ in blue. The normalized integral difference (NID) is the maximum difference between the two integrals.

mLCE data, we are able to obtain a conservative prediction of how much chaoticity is preserved without needing to run mLCE phase space maps, which take hours to generate.

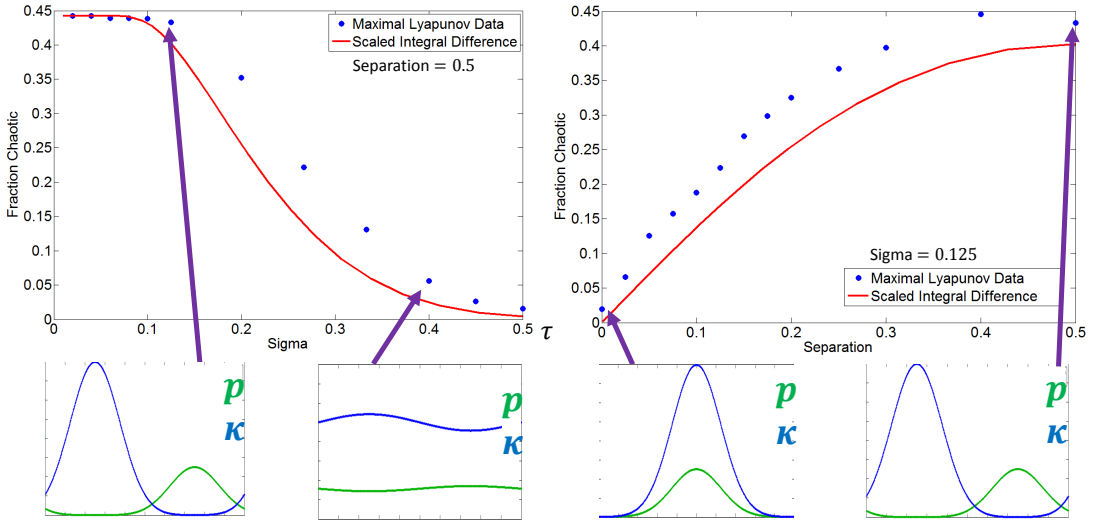

FIGURE F.6: Scaled NID plotted against the percentage of chaoticity found in mLCE maps. We see that the scaled NID is a good model for approximating how perturbations in pulse width and separation can affect the chaoticity of the kicked top system.

Bibliography

[1] P. Roushan. Observation of topological transitions in interacting quantum circuits. *Nature*, 515:241, Jun 2014. doi: 10.1038/nature13891. URL http://www.nature.com/nature/journal/v515/n7526/abs/nature13891.html.

[2] R. Barends. Digital quantum simulation of fermionic models with a superconducting circuit. *Pre-print*, 2015. URL http://arxiv.org/abs/1501.07703.

[3] C. Neill. Ergodic dynamics and the resulting thermalization in an isolated quantum system. *Pre-print*, 2015.

[4] CoaxCo Japan. Superconducting semi-rigid coaxial cable. http://old.coax.co.jp/english/news/SC-219-50-NbTi-NbTi_leaflet.pdf.

[5] Rami Barends. Minimizing quasiparticle generation from stray infrared light in superconducting quantum circuits, http://web.physics.ucsb.edu/~martinisgroup/papers/Barends2011.pdf. *Applied Physics Letters*, 99:113507, 2011. URL http://scitation.aip.org/content/aip/journal/apl/99/11/10.1063/1.3638063.

[6] Kurtis Lee Geerlings. *Improving Coherence of Superconducting Qubits and Resonators*, *http://qulab.eng.yale.edu/documents/theses/Kurtis_ImprovingCoherenceSuperconductingQubits.pdf*. PhD thesis, Yale University. Pg 83-89, 2013.

[7] Emerson and Cumming. Mf technical bulletin. http://www.eccosorb.com/Collateral/Documents/English-US/MF.pdf, 2008.

[8] David M. Pozar. *Microwave Engineering 4th Ed.* 2012. Pg 51, 54.

[9] R. Barends. Coherent josephson qubit suitable for scalable quantum integrated circuits. *Phys. Rev. Lett.*, 111:080502, Aug 2013. doi: 10.1103/PhysRevLett.111.080502. URL http://link.aps.org/doi/10.1103/PhysRevLett.111.080502.

[10] Yu Chen. Qubit architecture with high coherence and fast tunable coupling. *Phys. Rev. Lett.*, 113:220502, Nov 2014. doi: 10.1103/PhysRevLett.113.220502. URL http://link.aps.org/doi/10.1103/PhysRevLett.113.220502.

[11] S. Chaudhury. Quantum signatures of chaos in a kicked top. *Nature*, 461, 2009.

[12] F. Haake. Lyapunov exponents from quantum dynamics. *Annalen der Physik*, 1992.

[13] M. Murison. Notes on how to numerically calculate the maximum lyapunov exponent. 1995.

[14] S. Filipp. Qubit manipulation and rotating wave approximation, http://qudev.ethz.ch/content/courses/QSIT12/QSIT12_qubitmanipulation.pdf. 2012.

[15] M. Sandri. Numerical calculations of lyapunov exponents. *The Mathematica Journal*, 6, 1996. URL http://www.mathematica-journal.com/issue/v6i3/article/sandri/.